Title

A Similarity Solution for Two-Phase Water,Air, and Heat Flow near a Linear Heat Source in a Porous Medium

Journal

Journal of geophysical research, 97(B2)

Authors

Doughty, C.
Pruess, K.

Publication Date

1991

LBL-30051
Preprint

Lawrence Berkeley Laboratory
UNIVERSITY OF CALIFORNIA

EARTH SCIENCES DIVISION

Submitted to International Journal of Heat
and Mass Transfer

A Similarity Solution for Two-Phase Water, Air, and Heat Flow near a Linear Heat Source in a Porous Medium

C. Doughty and K. Pruess

January 1991

Prepared for the U.S. Department of Energy under Contract Number DE-AC03-76SF00098.

DISCLAIMER

LBL-30051

A Similarity Solution for Two-Phase Water, Air, and Heat Flow near a Linear Heat Source in a Porous Medium

Christine Doughty and Karsten Pruess

Earth Sciences Division
Lawrence Berkeley Laboratory
University of California
Berkeley, California 94720

January 1991

This work was carried out under U.S. Department of Energy Contract No. DE-AC03-76SF00098, through the Yucca Mountain Project, Sandia National Laboratories, under Document No. SNL 54-1065; numerical computations were supported by the Director, Office of Energy Research, Office of Basic Energy Sciences, Engineering and Geosciences Division, of the U.S. Department of Energy.

LBL-30051

A Similarity Solution for Two-phase Water, Air, and Heat Flow near a Linear Heat Source in a Porous Medium

Christine Doughty and Karsten Pruess

Earth Sciences Division

Lawrence Berkeley Laboratory

January 1991

Abstract

A recently-developed semianalytical solution for two-phase flow of water and heat in a porous medium has been extended to include an air component, and to incorporate a number of physical effects that broaden its range of applicability. The problem considered is a constant-strength linear heat source emplaced in an infinite homogeneous medium with uniform initial conditions. Under these conditions the governing partial differential equations in radial distance r and time t reduce to ordinary differential equations through the introduction of a similarity variable $\eta = r/\sqrt{t}$. The resulting equations are coupled and nonlinear, necessitating a numerical integration. The similarity solution developed here is used to investigate various physical phenomena related to partially saturated flow in low permeability rock, such as vapor pressure lowering, pore-level phase change effects, and an effective-continuum representation of fractured/porous media. The solution is compared to a numerical finite-difference scheme, and several illustrative applications to problems arising in the context of high-level nuclear waste disposal are given.

Nomenclature

b	Klinkenberg factor (Pa) (Eq. 20)
c	specific heat (J/kg K)
D_w, D_a	vapor and air diffusion coefficients (m^2/s) (Eqs. 18, 19)
D_{va}^0	binary diffusion strength in free gas at reference conditions of $P = 1$ bar, $T = 0°C$ (m^2/s) (Eqs. 18, 19)
h	enthalpy (J/kg)
K	mobility (kg/s m Pa) ($K_j = kk_{rj}\rho_j/\mu_j$, $j = l, g$)
k	intrinsic permeability (m^2)
$\tilde{k}$	effective-continuum intrinsic permeability (m^2) (Eq. 7)
k_r	relative permeability
$\tilde{k}_r$	effective-continuum relative permeability (Eq. 13)
P	pressure (Pa)
P_c	capillary pressure (Pa) ($P_c = P_l - P_g$)
Q_e	heat flow rate (W/m)
Q_w, Q_a	mass flow rates (kg/s m) ($Q_m = Q_l^m + Q_g^m$, $m = w, a$)
r	radial distance (m)
S	saturation
$\tilde{S}$	effective-continuum saturation (Eq. 12)
S_{lr}	residual liquid saturation
S_{crit}	critical liquid saturation (Eq. 14 and Table 3); in concurrent-saturation model, saturation above which fracture capillary pressure is zero
S_{th}	threshold liquid saturation (Eq. 15); in sequential-saturation model, saturation at which matrix is fully saturated and fractures are completely dry
T	temperature (°C)
t	time (s)
u	internal energy (J/kg)
V_m, V_f	fractional volume of matrix and fracture ($V_m + V_f = 1$)
X	mass fraction
z	integration variable ($z = \ln(\eta)$)

Greek Symbols

β	constant of order one in vapor diffusion coefficient (Eq. 19)
ε	relative error during numerical integration
η	similarity variable ($\eta = r/\sqrt{t}$)
θ	temperature exponent in vapor and air diffusion coefficients (Eqs. 18, 19)
κ	thermal conductivity (W/m K)
λ	parameter in van Genuchten characteristic curves
μ	dynamic viscosity (Pa s)
ρ	density (kg/m^3)
ϕ	porosity
$\tilde{\phi}$	effective-continuum porosity (Eq. 8)
τ	tortuosity (Eqs. 18, 19)

Subscripts

a	air (also used as a superscript)
c	capillary
e	energy
f	fracture
g	gas phase
L	lower limit of integration
l	liquid phase
m	matrix
r	relative
sat	at saturation (vapor-liquid equilibrium)
s	solid
th	threshold
U	upper limit of integration
v	vapor
w	water (also used as a superscript)
0	boundary condition, reference value

1. Introduction

We have developed a semianalytical solution for transient two-phase water, air, and heat flow in a porous medium surrounding a constant-strength linear heat source, using a similarity variable $\eta = r/\sqrt{t}$. While the similarity transformation approach requires a simplified geometry, all the complex physical mechanisms involved in coupled two-phase fluid and heat flow can be taken into account in a rigorous way, so the solution may be applied to a variety of problems of current interest. Application of the similarity variable approach to two-phase fluid and heat flow problems in radial geometry was pioneered in the geothermal well test studies of Grant [1979] and O'Sullivan [1981]. Grant developed a quasi-analytic approach for the analysis of geothermal wells producing from two-phase reservoirs, using an approximate linearization of the governing equations. O'Sullivan recognized that the similarity variable concept can be used to obtain solutions that include all nonlinearities of the governing equations in a rigorous way. Our work was motivated by a desire to predict the thermohydrological response to the proposed geologic repository for heat-generating high-level nuclear wastes at Yucca Mountain, Nevada, in a partially-saturated, highly-fractured volcanic formation. The geometric simplifications required by the similarity solution preclude rigorous predictions of the behavior of the repository as a whole, but the solution can be used to gain insight into the impact of various flow and heat transport parameters on physical conditions near the waste canisters. Other problems that can be studied involve heat sources such as buried power-transmission cables, volcanic dikes, agricultural root-zone heating operations, and underground thermal energy storage systems. Furthermore, the ability to rigorously solve a class of highly nonlinear two-phase fluid and heat flow problems has important applications in the verification of complex numerical simulators.

A previous paper [Doughty and Pruess, 1990] described the governing equations and methodology of our semianalytical similarity solution. Applications were demonstrated for simplified problems that did not include air, and had a constrained form for the characteristic curves (relative permeability and capillary pressure as a function of liquid saturation). The present work retains the basic conceptual model and methodology of the previous work, but presents a considerable enhancement of the flexibility and applicability of the similarity solution. One of the strengths of the similarity variable approach is the ability to study a variety of physical processes within a single framework. Among the improvements are incorporation of (i) an air component, (ii) more general characteristic curves, including an effective-continuum representation of fractured/porous media, (iii) vapor pressure lowering effects, (iv) enhanced

vapor diffusion arising from pore-level phase change effects, and (v) an approximate treatment of Knudsen diffusion using the Klinkenberg b factor.

2. Thermal and Hydrologic Conditions near the Heat Source

The fluid and heat flow problem is posed in the context of the proposed nuclear waste repository at Yucca Mountain, Nevada. The ambient temperature in the partially saturated formation around the repository ($T_0 \approx 20°$ C) is well below the saturation temperature at ambient pressure ($T_{sat} \approx 96°$C at $P_0 \approx 0.89$ bars) so water is primarily in the liquid phase, and the initial heat transfer in the host rock is mainly conductive. As the temperature around a waste package (the heat source) increases to the saturation temperature, evaporation increases and vapor partial pressure becomes appreciable. A convective heat-transfer mechanism with counter-flow of liquid and gas phases, known as a heat pipe, may contribute to or even dominate heat transfer in this regime. Near the heat source, liquid water vaporizes, causing pressurization and an out-flow of the gas phase. The water vapor condenses in cooler more distant regions, depositing its latent heat of vaporization. This creates a nonuniform saturation profile, with liquid saturation increasing with distance from the heat source. The saturation gradient drives the counter-flow of the liquid phase toward the heat source through capillary forces. The liquid then vaporizes again and repeats the cycle. With time the heat pipe moves away from the waste canister, leaving a gas-phase zone in which heat transfer is again conduction-dominated. The convective heat transfer of the heat-pipe region is accompanied by small temperature gradients, whereas in the conductive regions temperature gradients are large. Thus, conditions at the waste package may vary greatly depending on the relative importance of conductive and convective heat transfer. If an extensive heat pipe develops, the temperature will remain near the saturation temperature (about 100°C) for long times. Under these conditions, air will be purged from the near-canister region, leaving a gas phase composed purely of water vapor (steam). If heat transfer is primarily conductive, a gas-phase zone, or two-phase zone with only a small amount of immobile liquid, will develop around the waste package. Temperatures may be very high and air is more likely to be present.

The basic requirements for heat-pipe development are (1) the presence of a volatile fluid and (2) a mechanism by which gas-phase fluid can flow away from the heat source and liquid-phase fluid toward it. In the context of a geologic nuclear waste repository, (1) requires that the heat-generating capacity of the wastes, coupled with the low thermal conductivity of rock,

must raise the temperature near the canisters beyond the saturation temperature of water under prevailing pressure conditions. For gas-phase flow away from the heat source to occur, the far-field pressure must be lower than the pressure at the heat source. Both these conditions are readily met for a partially saturated repository environment ($P \approx 1$ bar), whereas for a deep water-saturated formation, in which fluid pressure at the waste packages is much greater than 1 bar and the far-field pressure is greater still, heat-pipe development is unlikely. Liquid-phase flow requires a driving force toward the heat source, which could be gravity, capillary pressure, or a combination of both. Finally, there must be sufficient permeability to both phases to establish the counter-flow necessary for a heat pipe. A fractured/porous medium may provide a combination of high gas-phase permeability through the fractures and strong capillary pressure in the rock matrix that facilitates heat pipe development. Theoretical and lab-scale experimental studies [Jennings and Udell, 1985] have shown that heat-pipe effects are greatly enhanced in heterogeneous porous media with coarse-grained and fine-grained materials arranged in parallel.

3. Methodology

The governing equations for two-phase fluid and heat flow for water and air in a porous medium are summarized in Appendix A. The basic processes represented by the equations are outlined below; further details may be found in Doughty and Pruess [1990]. A conservation law balances accumulation and flux of each component (water, air, energy), assuming local thermodynamic equilibrium between water, air, and rock. The fluid flux terms include Darcy's law modified for two-phase flow using relative permeability and capillary pressure functions, and binary diffusion between water vapor and air in the gas phase. The inclusion of capillary pressure ($P_c = P_l - P_g$) allows the possibility of liquid and gas phase counter-flow. Both the relative permeability and capillary pressure functions are highly nonlinear functions of liquid saturation. The heat balance includes conductive and convective terms with phase-change effects and transport of latent heat. Realistic equations of state for water [International Formulation Committee, 1967] and air (ideal gas with Henry's law for dissolution in the liquid phase) are used. With these assumptions, the conservation laws form a set of three coupled nonlinear second-order partial differential equations, which are mathematically equivalent to a set of six nonlinear coupled first-order partial differential equations. For single-phase conditions, the six primary dependent variables (unknowns) are temperature T, pressure P, air partial pressure P_a, water flux Q_w, air flux Q_a, and heat flux Q_e. Under two-phase conditions, gas saturation S_g

replaces T as a primary variable, as temperature can be determined directly from other primary variables through the saturation curve and a vapor pressure lowering correction. In some contexts it is more natural to consider liquid saturation as the primary variable, but this poses no problem as S_g and S_l are simply related by $S_g + S_l = 1$. Due to the inclusion of capillary pressure, under two-phase conditions it is necessary to choose either P_g or P_l as the primary variable; by convention we take P_g. Under single-phase conditions no such distinction is needed, and pressure is simply referred to as P.

To achieve the geometric symmetry required for the similarity variable approach, the geologic medium is assumed to be uniform and isotropic, the heat source is modeled as an infinitely long cylinder, and gravity is neglected. The geometry of the problem is then reduced to radial symmetry, with just two independent variables, radial distance r and time t. If the medium is of infinite extent with uniform initial conditions, and boundary conditions are applied only at $r = 0$ (a line source) and $r = \infty$, and are time-independent, the partial differential equations can be transformed into simpler ordinary differential equations (ODEs) through the use of a similarity variable, $\eta = r/\sqrt{t}$. This transformation is known as the Boltzmann transformation in the context of heat-conduction problems, and has been applied by Grant [1979] and O'Sullivan [1981] to geothermal well test problems.

The resulting ODEs are still coupled and nonlinear, so a numerical integration from $\eta = 0$ to $\eta = \infty$ is required to solve them. It proves to be convenient to use $z = \ln(\eta)$ as the integration variable. For the linear heat source representing a backfilled or 'closed-hole' nuclear waste canister, the boundary conditions are

$$z = \ln(\eta) = \ln(r/\sqrt{t}) = -\infty \qquad (r = 0 \text{ or } t = \infty) \tag{1}$$

$$Q_w = 0 \qquad Q_a = 0 \qquad Q_e = Q_{e0}$$

$$P,\ P_a,\ T \text{ unknown}$$

and

$$z = \ln(\eta) = \ln(r/\sqrt{t}) = +\infty \qquad (r = \infty \text{ or } t = 0) \tag{2}$$

$$P_g = P_0 \qquad P_a = P_{a0} \qquad S_g = S_0$$

$$Q_w,\ Q_a,\ Q_e \text{ unknown.}$$

Note that Equation (1) implies single-phase gas conditions exist at $z = -\infty$, while Equation (2) implies two-phase conditions exist at $z = +\infty$. Based on the discussion of Section 2, this is the

most likely scenario, but other conditions can be treated as well, with a suitable choice of primary variables. The boundary conditions given by Equations (1) and (2) constitute a two-point boundary value problem in which three of the boundary conditions are specified at the $z = -\infty$ limit of integration, and three at the $z = +\infty$ limit. The ODEs in z set up a functional dependence between the upper and lower boundary conditions, requiring an iterative process for solution. We use an iterative integration scheme, known as the shooting method [Press et al., 1986], which consists of a Newton-Raphson iteration on the unknown boundary conditions $(P, P_a, T)|_{z=-\infty}$. For the numerical integration, the limits $z = \pm\infty$ are replaced by finite values z_L and z_U (see below). At the lower limit of the integration, values are guessed for the missing boundary conditions, and the numerical integration of the coupled ODEs is carried out. At the upper limit of the integration, the values of the variables are compared to the specified boundary conditions, and refined estimates of the lower limit boundary conditions are made. This procedure continues until the value of each variable at $z = z_U$ matches the specified boundary conditions P_0, P_{a0}, and S_0.

The numerical integration is done using a fourth order Runge-Kutta integration scheme. Integration step size is determined adaptively via Richardson extrapolation: step size is adjusted so that the results of two half steps agree with the results of one whole step, with a user-specified error ε. The value of ε necessary to get accurate results at z_U depends strongly on the nature of the problem.

4. Incorporation of an Air Component

The illustrative results of the similarity solution presented in Doughty and Pruess [1990] treated a one-component two-phase fluid (water, present as liquid or vapor) saturating the formation surrounding the repository, and required solving a set of four coupled first-order differential equations. The incorporation of an air component increases the number of equations from four to six, and although this significantly increases the number of computations required, there is no essential conceptual difference between the similarity solution methodology for problems with and without air.

In practice, the coupling between the various equations becomes more complicated when air is included, requiring more careful use of the iterative procedure within the similarity solution. Additionally, at the lower limit of the integration the air partial pressure $P_a(z_L)$ is nearly zero for a fully-developed heat pipe. However, P_a is used as a shooting variable, requiring that

distinct, nonzero values be supplied to start the numerical integrations of the ODEs at $z = z_L$. Due to binary diffusion, there is a nonzero air partial pressure everywhere (including z_L), but $P_a(z_L)$ can be extremely small for a long heat pipe. This leads to stringent numerical accuracy requirements ($\varepsilon \leq 10^{-6}$), and correspondingly higher computing effort. Neither of these complications causes a failure of the similarity solution, but they do preclude its use as a 'black box'. Judicious choice of starting values for the ODE integrations and some trial and error is required to achieve convergence of the Newton-Raphson iteration.

Figure 1 shows results for two problems which are identical except for the presence or absence of air. For convenience, air mass fraction X_g^a is plotted instead of P_a. Most of the parameters used to specify these problems, given in Table 1, are typical of conditions expected at the proposed nuclear waste repository at Yucca Mountain [Pruess et al., 1990a]. However, fracture effects are not included, and intrinsic permeability of the intact rock matrix is extremely low. Therefore, in order to illustrate a stronger heat pipe, intrinsic permeability has been arbitrarily increased by a factor of order 10,000, to 20×10^{-15} m^2, and for consistency capillary pressure has been reduced by a factor $\sqrt{10{,}000} = 100$ in comparison to typical Yucca Mountain data.

According to the definition of the similarity variable, $z = \ln(r/\sqrt{t})$, Figure 1 represents both a spatial distribution at a given time, with distance from the heat source increasing from left to right, and a time sequence at a given point in space, with time increasing from right to left. Most of the discussion of figures that follow is done in terms of a spatial distribution. Overall the "with-air" and "no-air" problems show quite similar results. Of course, for the no-air problem, single-phase liquid conditions exist far from the heat source ($S_l = 1$ for $z > -8$), whereas the with-air problem is two-phase ($S_l = 0.8$), but the pressure and temperature profiles are not very different. The constant pressure and steep linear temperature profiles shown in Figure 1a for $-10 < z < -8.5$ and $-8 < z < -6.5$ indicate conductive regimes, and Figure 1b verifies that mass flow rates are small there. The more gradual temperature decline for $-8.5 < z < -8$ coupled with a large liquid-vapor counter-flow identifies the heat-pipe region. In Figure 1b, Q_g and Q_l are the sum of the air and water components for the gas and liquid phases, respectively. Throughout this paper, the scale on which the mass flows are shown makes air flow vanishingly small, so the mass flow for each phase is essentially water flow (e.g., $Q_g = Q_v$). Note that air mass fraction X_g^a is essentially zero for $z < -8$, so the gas phase there is composed primarily of water vapor (at $z_L = -11$, $X_g^a = 10^{-24}$). The air is purged from

the near heat source region by the vapor flow away from the heat source. This could have important ramifications for waste-package design with regard to the prevention of corrosion. Extending from the cool end of the heat pipe to the heat-flow front ($-8.2 < z < -6$), there is a small liquid flow away from the heat source. This out-flow is necessary because the water vapor forming at the hot end of the heat pipe is much less dense than the liquid water it replaces.

Generally, the presence of air shortens the heat pipe from the cold end, by hampering the liquid-vapor counter-flow there. When air is present at the cold end of the heat pipe, liquid flow is decreased there because liquid relative permeability is lower due to the smaller liquid saturation. Vapor flow is decreased because for a given pressure gradient and gas-phase saturation only some of the mass flow is vapor, the rest being air. The heat-pipe shortening with the presence of air is evident from Figure 1, but it occurs at the hot end of the heat pipe. Because both the with-air and no-air solutions are constrained to match the same pressure and temperature boundary conditions at z_U, any difference in heat-pipe length is shifted toward z_L.

The physical processes associated with the addition of air can be demonstrated more clearly by doing a series of integrations using the no-air boundary conditions for $T(z_L)$ and $P(z_L)$, and sequentially increasing $P_a(z_L)$ from 0 to 10^{-41} to 10^{-26} bars (Figure 2). The boundary conditions at z_U are not matched, but the effect of adding air to shorten the heat pipe is clearly illustrated. Although these values of $P_a(z_L)$ are much too small to be readily distinguished experimentally, with sufficient numerical accuracy ($\varepsilon = 10^{-6}$) they can be used successfully in the similarity solution. This example demonstrates one of the attractive features of the similarity solution: its usual method of employment – taking initial guesses for missing boundary conditions from results of a similar problem – provides insight into the physical effects of various problem parameters.

Two other differences that arise from the presence of air are also illustrated in Figure 1. The pressure decrease that occurs over the length of the heat pipe is larger for the no-air problem because the heat pipe is longer. The pure liquid zone that develops for the no-air problem for $z > -8$ has a much lower compressibility than does the low temperature two-phase zone of the with-air problem, hence the small liquid out-flow extends much further from the heat source.

5. Comparison with the Numerical Simulator TOUGH2

Multiphase fluid and heat flow problems that lack some of the symmetries required for application of the similarity variable approach must be solved by numerical simulation, using discretization of the continuous space and time variables. The accuracy and credibility of numerical simulations is a matter of serious concern, because they are subject to space and time discretization errors which are often difficult to quantify. Furthermore, numerical simulations are performed with complex computer programs, and no method is known to directly establish that such programs are free of errors. It is necessary, therefore, to test numerical simulations against known solutions that entail as many complex features as possible. The similarity solution is an ideal tool for such testing, because it gives, within the approximations of the underlying mathematical model, a very accurate solution to a problem that involves the full nonlinear process complexity of transient two-phase fluid and heat flow. The idealizations made pertain only to the flow geometry, and to initial and boundary conditions.

We have used the similarity solution to test the numerical simulator TOUGH2 [Pruess, 1987, 1990], which calculates the flow of air and water in gaseous and liquid phases together with heat flow, using the same governing equations and equation of state as does the similarity solution. TOUGH2 employs the integral-finite-difference method to discretize space for one-, two-, or three-dimensional problems that may involve heterogeneous, anisotropic, or fractured/porous media [Narasimhan and Witherspoon, 1976]. Figure 3 shows results of TOUGH2 compared with those of the similarity solution for the problem specified in Table 1. The agreement is excellent. A one-dimensional radial mesh with 108 elements was used for the TOUGH2 calculation. The mesh spacing is nonuniform, with finest spacing (0.03 m) used where the similarity solution predicts sharp gradients. A heat source is placed in the innermost element ($0 < r < 0.3$ m), and the outermost element ($r = 10{,}000$ m) is at sufficiently large distance to remain at constant temperature, pressure, and saturation for a simulation time of 6.3 years. The TOUGH2 calculation required 800 time steps and 8.5 minutes of CPU time on the Cray X-MP at the National Energy Research Supercomputer Center at Lawrence Livermore National Laboratory.

In contrast, one numerical integration of the similarity solution, using previously-determined correct starting values at z_L and specifying a relative error $\varepsilon = 10^{-4}$, required 228 integration steps and took 2.6 CPU seconds. The shooting procedure requires four integrations per shot, and with reasonable initial guesses, usually converges within three to five shots. The

key to successful use of the similarity solution is finding reasonable initial guesses. This may require some preliminary trial integrations, the solution to a similar problem, physical intuition, or a combination of the three. Assuming five trial integrations to arrive at workable initial guesses, and four shots to find the solution, the whole procedure would require 21 shots, or an approximate CPU time of 55 seconds. This sample problem has a relatively short heat pipe, which makes accuracy requirements modest. A numerical integration specifying $\varepsilon = 10^{-2}$ gave the same results, but took only 106 steps, requiring 1.4 CPU seconds. Conversely, for a long heat pipe, greater accuracy is needed, and computation effort increases correspondingly.

6. Characteristic Curves with $S_{lr} > 0$

Our previous implementation of the similarity variable approach [Doughty and Pruess, 1990] had been limited to relative permeability curves that have a residual liquid saturation of zero ($S_{lr} = 0$). When $S_{lr} > 0$, a two-phase region exists in which liquid is immobile, which complicates the solution of the coupled differential equations, as described below. The similarity variable methodology involves expressing the governing equations in terms of derivatives of the primary variables, using the chain rule. The equations for heat and mass flux for two-phase conditions (Equations (A8) and (A9) in Appendix A) are of the form

$$Q_m = A_m \frac{dP_g}{dz} + B_m \frac{dS_g}{dz} + C_m \frac{dP_a}{dz} \qquad \text{for } m = w, a, e \tag{3}$$

and the conservation equations (Equation (A7) in Appendix A) are of the form

$$\frac{dQ_m}{dz} = \frac{e^{2z}}{2}\left[D_m \frac{dP_g}{dz} + E_m \frac{dS_g}{dz} + F_m \frac{dP_a}{dz}\right] \qquad \text{for } m = w, a, e \tag{4}$$

where A_m, B_m, C_m, D_m, E_m, and F_m are functions of P_g, S_g, and P_a. We would like to solve the three equations given by Equation (3) for the unknowns dP_g/dz, dS_g/dz, and dP_a/dz, then subsequently substitute these expressions into Equation (4) and thereby determine dQ_w/dz, dQ_a/dz, and dQ_e/dz. When vapor pressure lowering is neglected, the coefficients B_m of dS_g/dz in Equation (3) are all proportional to the liquid mobility K_l. Then if $S_l < S_{lr}$ so that $K_l = 0$, it is not possible to solve these equations for dS_g/dz. One solution to this problem is to include vapor pressure lowering, which makes B_e nonzero for all values of S_l. This approach is used in the following section. For the no-vapor-pressure-lowering case, a more complicated scheme was developed to solve the conservation and flux equations simultaneously for the hypothesized finite z domain in which $0 < S_l < S_{lr}$. Surprisingly, it indicated that

dS_g/dz should be positive, which does not make sense because S_g starts out at one, so cannot increase. Therefore an alternative, less formal approach was taken to the problem.

Figure 4a shows some hypothetical liquid relative permeability curves $k_{rl}(S_l)$ for the case $S_{lr}=0$, calculated using the formula given in Table 1. Actual liquid relative permeability curves found in the soil science, petroleum, and hydrogeological literature [e.g. van Genuchten, 1980; Corey, 1954; Verma et al., 1985] are usually strongly concave up, i.e., $k_{rl}(S_l) \ll S_l$, as shown in the $\lambda=0.95$ and $\lambda=0.45$ curves in Figure 4a. Figure 4b shows the similarity solution results obtained using these k_{rl} functions, for a no-air problem. Note that as λ decreases (i.e., the value of k_{rl} for a given value of S_l decreases) the initial slope of the saturation profile becomes steeper. This variation confirms an approximate result from Doughty and Pruess [1990, Section 6.1], which predicted that for small values of S_l,

$$\frac{dS_l}{dz} \sim \frac{1}{k_{rl}}. \tag{5}$$

If we extrapolate to $k_{rl}=0$ (i.e., $S_{lr}>0$), the initial slope of the saturation profile becomes essentially infinite. Effectively, there will be a jump in the saturation profile between the $S_l=0$ value for the single-phase gas region, and $S_l=S_{lr}$ in the two-phase region, occurring at a single value of z. The dependence of dS_l/dz on $1/k_{rl}$ reflects the need for sufficient liquid counterflow to maintain a heat pipe, as a large value of dS_l/dz indicates a rapid transition from a heat-pipe region to a conductive region. This argument is based on no-air calculations, but Figure 1a has shown that the addition of air does not change the shape of the initial portion of the saturation profile.

In terms of the numerical integration in z, the discontinuity in S_l amounts to skipping the region $0<S_l<S_{lr}$, and going directly from a single-phase gas region to a two-phase region where liquid is mobile, with a discontinuous jump from $S_l=0$ to $S_l \geq S_{lr}$ at a single value of z. This discontinuity in the saturation profile explains why our attempted special solution scheme for $0<S_l<S_{lr}$ did not work: there is no finite z domain for which $0<S_l<S_{lr}$.

The saturation-jump hypothesis has been substantiated by examining the saturation profiles calculated by the numerical model TOUGH2 for cases with $S_{lr}>0$, which show very nearly vertical saturation profiles for $S_l<S_{lr}$. Of course, sharp profiles are difficult for numerical models to calculate accurately, as numerical dispersion widens fronts, so the TOUGH2 results represent corroboration, not proof, of the hypothesis.

7. Vapor Pressure Lowering

Under two-phase conditions, the primary thermodynamic variables are gas-phase pressure P_g, gas saturation S_g, and air partial pressure P_a. When vapor pressure lowering effects are ignored, temperature is determined iteratively from the steam table saturation curve $P_v = P_{sat}(T)$. Since $P_v = P_g - P_a$, the functional dependence of temperature on the primary variables is $T = T(P_g, P_a)$. Vapor pressure lowering is modeled using the Kelvin equation, so the temperature becomes a function of saturation as well as vapor pressure, given implicitly by

$$P_v = P_{sat}(T) \cdot \exp\left[\frac{P_c(S_l)}{\rho_l R (T + 273.15)}\right] \tag{6}$$

Thus the functional dependence of temperature on the primary variables is $T = T(P_g, P_a, S_g)$. The presence of a nonzero $\partial T / \partial S_g$ term in Equation (3) ensures that B_e does not vanish (see Equation (A9) in Appendix A), so Equation (3) can be uniquely solved for dP_g/dz, dS_g/dz, and dP_a/dz whether or not $K_l = 0$.

In the previous section it was determined that for the no-vapor-pressure-lowering case, the increase from $S_l = 0$ to $S_l = S_{lr}$ occurs as a discontinuous jump at a single value of z. In contrast, our calculations indicate that for strong vapor pressure lowering, the region where $0 < S_l < S_{lr}$ may be quite extensive (see below), but as vapor pressure lowering becomes weaker and weaker (results not shown), this part of the saturation profile becomes sharper and sharper, approaching the discontinuous jump hypothesized in the previous section.

Figure 5 shows results for two problems which are identical except for the presence or absence of vapor pressure lowering. The parameters used to specify these problems, given in Table 2, are typical of the intact rock of the Yucca Mountain tuffs, with fracture effects not taken into account [Tsang and Pruess, 1990]. The primary differences from the problem described in Table 1 are a factor of order 10^4 decrease in intrinsic permeability and a factor of order 10^2 increase in capillary pressure strength. The weaker capillary pressure of the Table 1 problem makes vapor pressure lowering effects negligible in that case. The capillary pressure function, slightly modified from the van Genuchten [1980] formulation (see Appendix B), has the feature that P_c becomes very large and negative as $S_l \to S_{lr}$. Then, from Equation (6), vapor pressure lowering effects become very strong for small S_l, and the two-phase region extends all the way to z_L, as is verified by Figure 5a. Except for this extension of the two-phase zone to small values of z, the results of the two problems are quite similar. The slope of the conductive temperature profile for $-11 < z < -10$ decreases slightly for the vapor-

pressure-lowering case, reflecting the increase in thermal conductivity with liquid saturation ($\kappa \sim \sqrt{S_l}$). For these problems, $S_l > S_{lr}$ throughout, but the intrinsic permeability is too small to allow enough fluid flow for much of a heat pipe to develop (Figure 5b), thus heat transfer is primarily conductive and the air component of the gas phase is not completely purged from the near heat source region (Figure 5a). With no vapor pressure lowering, the air mass fraction X_g^a is constant in the gas-phase region, whereas the additional coupling between T, P_g, and P_a that results from vapor pressure lowering causes X_g^a to decrease slightly for $-11 < z < -10$.

Usually when two-phase conditions prevail at z_L, the initial values for the numerical integration are specified in terms of P_g, P_a, and S_g. However, when conditions at z_L are two-phase due to strong vapor pressure lowering, the value of $S_g(z_L)$ can vary greatly, making it difficult to make good initial guesses. In fact, for a capillary pressure function that does not have the feature $|P_c| \to \infty$ as $S_l \to 0$, one does not know *a priori* what phase conditions exist at z_L. To deal with this problem, the similarity solution allows initial guesses to be made in terms of single-phase variables (P_g, P_a, T), which are internally converted to two-phase variables if vapor pressure lowering is strong enough to maintain two-phase conditions at z_L. This conversion procedure also makes it convenient to solve a no-vapor-pressure-lowering version of a problem first, then add vapor pressure lowering.

8. Effective Continuum Representation of a Fractured/Porous Medium

A variety of methods are currently being used to mathematically model fractured geologic media, including explicit discretization of the fractures, double or multiple porosity models, and effective-continuum representations. Of these three, only the last is useful within the similarity transformation context, because of the requirement of a single homogeneous, isotropic medium. In the effective-continuum approach, a single continuous medium incorporates features of both the fractures and the intact rock matrix, through the use of a particular set of characteristic curves. To motivate the form of these characteristic curves a brief discussion of the nature of two-phase fluid flow in fractured/porous media is presented below. A more detailed description may be found in Wang and Narasimhan [1985]. Conditions for the applicability of an effective-continuum approximation have been derived by Pruess et al. [1990b].

Generally, in a partially saturated geologic medium, liquid water is the wetting phase and the vapor-air mixture making up the gas phase is the non-wetting phase, implying that the gas phase occupies the larger pores, while the liquid phase occupies the smaller pores as well as

forming a film on mineral surfaces. The capillary pressure is inversely proportional to the radius of curvature of the interface between the two phases, and the radius of curvature increases with liquid saturation S_l as the liquid occupies pores of larger radius. In a fractured/porous medium the pore spaces within the rock matrix are usually much smaller than the fracture apertures separating blocks of rock. Under conditions of capillary pressure equilibrium between the rock matrix and fractures, liquid water then preferentially occupies the pore spaces of the rock matrix and the gas phase preferentially occupies the fractures. The actual values of the liquid saturations in the matrix and fractures are often poorly known as they depend not only on the mean pore and aperture sizes, but on such complicated factors as the distributions of pore and aperture sizes, adsorption properties which may differ for fractures and pore spaces, and whether wetting or drying is occurring. However, knowledge of liquid saturation is crucial to predicting fluid flow, because although the fractures have an intrinsic permeability orders of magnitude higher than that of the rock matrix, liquid relative permeability may be orders of magnitude less than one for low values of liquid saturation, essentially precluding liquid flow within the fractures.

To use the effective-continuum formulation in the similarity solution, suitable 'effective' values of material properties and primary variables need to be defined. The effective intrinsic permeability and porosity are given by

$$\tilde{k} = k_m V_m + k_f V_f \tag{7}$$

$$\tilde{\phi} = \phi_m V_m + \phi_f V_f \tag{8}$$

where the subscripts m and f refer to matrix and fracture, respectively, and V is fractional volume ($V_m + V_f = 1$). Equation (7) assumes that permeabilities of fractures and rock matrix act in parallel.

The rock matrix and fractures are assumed to be in local thermodynamic equilibrium, so locally all thermodynamic variables take on the same value whether in rock matrix or fracture (e.g., $T_m(r,t) = T_f(r,t)$). For single-phase conditions, the primary variables P, T, and P_a are all thermodynamic variables, so may be used directly as effective primary variables. Under two-phase conditions, S_g replaces T as a primary variable. However, S_g is not a thermodynamic variable, and it is not generally true that $S_{gm} = S_{gf}$. Thermodynamic equilibrium does hold for both liquid and gas phase pressures

$$P_{gm} = P_{gf} \tag{9}$$

$$P_{lm} = P_{lf} \tag{10}$$

and with the usual relation between liquid and gas phase pressures, $P_l = P_g + P_c$, Equations (9) and (10) may be combined to obtain $P_{cm} = P_{cf}$. Recent experimental and theoretical studies have suggested that the capillary pressure behavior of fractures under desaturation may not be much different from that of porous media, except that fracture capillary pressures tend to be weaker [Firoozabadi and Hauge, 1990; Pruess and Tsang, 1990]. Thus in principle, one can determine functional forms $P_{cm}(S_{lm})$ and $P_{cf}(S_{lf})$ to describe capillary pressure variation with saturation in matrix and fractures, respectively. Then the thermodynamic equilibrium requirement

$$P_{cm}(S_{lm}) = P_{cf}(S_{lf}) \tag{11}$$

provides an implicit means of relating matrix and fracture liquid saturations S_{lm} and S_{lf}. An effective primary variable may then be defined as $\tilde{S}_g = 1 - \tilde{S}_l$, where

$$\tilde{S}_l = \frac{S_{lm}\phi_m V_m + S_{lf}\phi_f V_f}{\tilde{\phi}}. \tag{12}$$

The final material properties needed to complete the effective-continuum formulation are the effective-continuum relative permeabilities, given by [Pruess et al., 1990b]

$$\tilde{k}_{rl} = \frac{k_m V_m k_{rlm}(S_{lm}) + k_f V_f k_{rlf}(S_{lf})}{\tilde{k}} \tag{13}$$

$$\tilde{k}_{rg} = 1 - \tilde{k}_{rl}$$

where k_{rlm} and k_{rlf} are liquid relative permeabilities in the matrix and fractures, respectively.

Thus, although the similarity variable approach uses $\tilde{S}_g$ as a primary variable to integrate, S_{lm} and S_{lf} also must be known at each step in the integration, so that P_c, $\tilde{k}_{rl}$, and $\tilde{k}_{rg}$ can be determined. Two alternative approaches have been developed to determine S_{lm} and S_{lf}: 1) a direct implementation of the assumption of capillary pressure equilibrium, known as the 'concurrent-saturation model' and 2) a simpler approximate treatment, known as the 'sequential-saturation model,' in which it is assumed that liquid can be present in the fractures only when the matrix is completely saturated. The basic features of each approach are described below, followed by a detailed description of its implementation in the similarity solution.

In the concurrent-saturation model, for each value of $\tilde{S}_g = 1 - \tilde{S}_l$ encountered during the numerical integration, Equations (11) and (12) are solved iteratively to determine S_{lm} and S_{lf}. If the fracture and matrix capillary pressures are of similar magnitude, Equation (11) implies that liquid saturation in the fractures increases or decreases concurrently with the liquid saturation in the matrix. On the other hand, if fracture capillary pressures are much weaker than those in the matrix, then Equation (11) implies that during wetting the matrix will become almost completely saturated before any liquid enters the fractures, and during drying the fractures will almost completely desaturate before any liquid leaves the matrix. Under these conditions, then, to a good approximation one may consider that water will be present in the fractures only when the matrix is completely saturated. This is the approach of the sequential-saturation model. It is easier to implement than the concurrent-saturation approach because S_{lm} and S_{lf} can be determined from $\tilde{S}_g$ using simple closed-form expressions, rather than an iterative procedure.

Approximate Treatment of the Concurrent-Saturation Model

In the concurrent-saturation approach, for a given value of $\tilde{S}_l$, Equations (11) and (12) are solved iteratively to determine S_{lm} and S_{lf}, which in turn determine $\tilde{k}_{rl}$ and $\tilde{k}_{rg}$ through Equation (13). This procedure could be done within the similarity solution, but the requirement for such an iteration every time a new value of $\tilde{S}_l$ is encountered (11 times per step of the ODE integration, using the Runge-Kutta scheme) would substantially increase computational effort. A more efficient approach is to use Equations (11), (12), and (13) in a separate iterative calculation to generate effective-continuum characteristic curves, then fit these curves with simple analytical forms to be used in the similarity solution. This technique, outlined below, is described in more detail in Doughty [1991].

Examples of $P_{cm}(S_{lm})$ and $P_{cf}(S_{lf})$ curves are shown in Figure 6. The functional forms and parameter values used to calculate P_{cm} and P_{cf} are given in Table 3. Because very little is known at present about fracture capillary pressures, we consider two cases which are intended to illustrate alternative possible system behavior. Following Pruess et al. [1990a], fracture capillary pressure P_{cf} is parameterized by a simple linear relationship

$$P_{cf}(S_{lf}) = P_{cm}(0)\cdot(1 - S_{lf}/S_{crit}) \qquad 0 < S_{lf} < S_{crit} \tag{14}$$

$$P_{cf}(S_{lf}) = 0 \qquad S_{crit} < S_{lf} < 1$$

which is constructed so that $P_{cm}(0) = P_{cf}(0)$ and $P_{cf}(1) = P_{cf}(1) = 0$. Note the $P_{cf} = 0$ for

$S_{lf} > S_{crit}$; however, the similarity solution algorithm requires non-zero values of dP_c/dz for all values of S_l. This is achieved by replacing $P_{cf} = 0$ for $S_{lf} > S_{crit}$ in Equation (14) with an extremely small linearly-varying value, see Table 3. As Figure 6 illustrates, requiring $P_{cm}(S_{lm}) = P_{cf}(S_{lf})$ implies $0 < S_{lf} < S_{crit}$ for most values of S_{lm}. In the first case considered, $S_{crit} < S_{lrf}$, so liquid will be immobile in the fractures unless $S_{lm} \approx 1$. In the second case, $S_{crit} > S_{lrf}$, so liquid can be mobile in the fractures for a wide range of S_{lm} values. In comparing these two limiting cases, it is apparent that the $S_{crit} < S_{lrf}$ case is consistent with the assumptions of the sequential-saturation model, whereas the $S_{crit} > S_{lrf}$ case is not.

Figure 7a shows the effective-continuum capillary pressure $P_c(\tilde{S}_l)$ calculated iteratively using the functions shown in Figure 6. Figure 7b shows the effective-continuum relative permeabilities $\tilde{k}_{rl}(\tilde{S}_l)$ and $\tilde{k}_{rg}(\tilde{S}_l)$ given by Equation (13), using the functional forms and parameter values from Table 3 for k_{rlm} and k_{rlf}, and the iteratively-determined values of S_{lm} and S_{lf}. Figure 7 also shows approximate closed-form expressions (given in Table 4) for the characteristic curves. From Figure 7b it is evident that whether or not $S_{crit} < S_{lrf}$ has a large effect on $\tilde{k}_{rl}$, which is not surprising considering the large contrast (10^7) between matrix and fracture permeabilities and the form of Equation (13). In contrast, Figure 7a shows that this small variation in S_{crit} does not have a noticeable effect on $P_c(\tilde{S}_l)$. In the next section it is shown that when $S_{crit} < S_{lrf}$, the closed-form solutions shown in Figure 7 can in fact be produced by the sequential-saturation model, validating its use under these conditions.

Sequential-Saturation Model

Following Tsang and Pruess [1990], a threshold liquid saturation S_{th} can be defined as the saturation at which the matrix is fully saturated and the fractures completely dry. From Equation (12), S_{th} is given by

$$S_{th} \equiv \tilde{S}(S_{lm} = 1,\ S_{lf} = 0) = \frac{\phi_m V_m}{\tilde{\phi}}. \tag{15}$$

When $0 < \tilde{S}_l < S_{th}$, the matrix is partially saturated and the fractures are fully desaturated

$$S_{lm} = \frac{\tilde{S}_l}{S_{th}} \qquad 0 < S_{lm} < 1 \tag{16}$$

$$S_{lf} = 0$$

$$P_c = P_{cm}\left[(1 - \delta_s)\tilde{S}_l / S_{th}\right].$$

When $S_{th} < \tilde{S}_l < 1$, the matrix is fully saturated and the fractures are partially saturated

$$S_{lm} = 1 \tag{17}$$

$$S_{lf} = \frac{\tilde{S}_l - S_{th}}{1 - S_{th}} \qquad 0 < S_{lf} < 1$$

$$P_c = \frac{1 - \tilde{S}_l}{1 - S_{th}} \cdot P_{cm}(1 - \delta_s).$$

The parameter δ_s is a small number ($\sim 10^{-4}$) introduced to represent capillary pressure at threshold saturation, $\tilde{S}_l = S_{th}$, where the matrix is fully saturated and the fractures are completely dry. The capillary pressure given by Equations (16) and (17) is illustrated in Figure 7a for the functional forms and parameter values from Table 4. With the proper choice of δ_s, it agrees within line width to the capillary pressure determined iteratively from Equations (11) and (12). Figure 7b shows the relative permeability curves given by Equation (13) using the functional forms and parameter values from Table 4 for k_{rlm} and k_{rlf}, and Equations (16) and (17) for S_{lm} and S_{lf}. The sequential-saturation model yields nearly identical relative permeability curves to the concurrent-saturation model when $S_{crit} < S_{lrf}$. On the other hand, when $S_{crit} > S_{lrf}$, the fracture contributes significantly to liquid relative permeability when $\tilde{S}_l < S_{th}$ ($S_{lm} < 1$). That is, liquid is mobile in the fractures before the matrix is fully saturated, which cannot be approximated by the sequential-saturation model.

Results for Effective Continuum

Figure 8 shows results of the similarity solution for a problem identical to that shown in Figure 5, except that fractures are included using the sequential-saturation model, with $V_f = 0.0018$, $k_f = 10^{-11}$ m^2, and $\phi_f = 1$ (problem parameters are summarized in Tables 2 and 4). Liquid saturation $\tilde{S}_l$ remains below the threshold value S_{th} everywhere, so liquid relative permeability is not enhanced by the fractures. Nonetheless, the fluid flow pattern changes markedly, with a short heat pipe now developing (compare Figures 5b and 8b). The enhanced gas-phase permeability not only allows increased gas-phase flow, but it substantially reduces the gas-phase pressure gradient, resulting in a large enough liquid-phase pressure gradient to drive a small liquid counter-flow ($dP_l/dz = dP_g/dz - dP_c/dz \approx -dP_c/dz$). Although the heat pipe is too short to create a flattening in the temperature profile (compare Figures 1a and 8a), it does effectively purge the air component of the gas phase from the near heat source region. The much smaller gas-phase pressure greatly decreases T_{sat} compared to the no-fracture case

(180 → 100°C), so the location of the de-saturation front (which occurs at $T=T_{sat}$) changes substantially, from $z=-10$ to $z=-8.2$ (compare Figures 5a and 8a). Because the far-field saturation is constrained by the boundary conditions to remain at $S_l=0.7$, the larger dried region is balanced by a "condensation halo", or region of increased saturation coincident with the cold end of the heat pipe.

It is of interest to note that for these matrix and fracture volumes and porosities the threshold saturation ($S_{th}=0.982$) is not much higher than the maximum liquid saturation in the condensation halo ($\tilde{S}_l=0.964$). With slightly different material properties, S_{th} could easily be decreased by a few percent. Our calculations indicate (results not shown) that the condensation halo of increased liquid saturation adjusts to remain just below the new value of S_{th}, producing results that look very similar to Figure 8. This occurs because the sharp saturation gradients in the condensation halo region give rise to strong capillary forces that drive fluid away from the halo in both directions. If $\tilde{S}_l > S_{th}$, the strongly increased liquid relative permeability due to the fracture component of $\tilde{k}_{rl}$ greatly facilitates such flow, decreasing the saturation back below S_{th}. Only if the threshold saturation is less than the far-field saturation ($S_{th} < S_{l0}$) does a substantially different picture emerge, with the saturation halo effectively dissipated and a much stronger counter-flow developing (Figure 9). This problem assumes the same parameters as the previous one, but a fracture volume of $V_f=0.05$ (much larger than the usual value taken for the Yucca Mountain site, $V_f=0.0018$), resulting in a threshold saturation of $S_{th}=0.65$, which is less than the far-field value of $S_{l0}=0.7$.

In both Figures 8 and 9 the no-vapor-pressure-lowering results are also shown. Just as in Figure 5, vapor pressure lowering causes an extension of two-phase conditions toward z_L, and a corresponding slight decrease in the slope of the temperature profile for $-11 < z < -8.5$. With vapor pressure lowering, the onset of counter-flow at the hot end of the heat pipe is gradual instead of abrupt, identifying an extended zone of evaporation.

The strong dependence of $\tilde{k}_{rl}$ on S_{crit} shown in Figure 7b indicates that the similarity solution may be strongly affected by this parameter. Figure 10 shows results of the similarity solution for a problem identical to that shown in Figure 8, except that a value of $S_{crit} > S_{lrf}$ is chosen to represent liquid that is just barely mobile in the fractures (characteristic curves are summarized in Table 4). The contrast between Figures 8 and 10 is great. When liquid can flow in both the fractures and the matrix an extended counter-flow region forms (Figure 10b) coincident with a marked flattening of the temperature profile (Figure 10a), resulting in

significantly lower temperature at the heat source. The condensation halo at the cold end of the heat pipe is much less pronounced, as liquid can flow away from the heat source more easily. The effect of vapor pressure lowering is also shown. In addition to extending the two-phase zone to small values of z, slightly decreasing the slope of the temperature profile there, and causing a gradually increasing counter-flow, as in Figures 7 and 8, here vapor pressure lowering actually extends the length of the heat pipe, by keeping $\tilde{S}_l > S_{lrf}$ for a larger range of z.

9. Enhanced Vapor Diffusion due to Pore-Level Phase-Change Effects

Diffusion between the water-vapor and air components of the gas phase is proportional to gradients in air mass fraction as shown in Equation (A8). The diffusion coefficients D_a and D_w represent the coefficient for diffusion of air in water vapor and the coefficient for diffusion of water vapor in air, respectively, in a porous medium. The coefficient D_a is given by [Vargaftik, 1975; Walker et al., 1981]

$$D_a = \tau\phi S_g D_{va}^0 \frac{P_0}{P}\left[\frac{T+273.15}{273.15}\right]^\theta \tag{18}$$

where τ is the tortuosity of the porous medium, D_{va}^0 is the diffusion coefficient of vapor and air in a free gas at reference conditions of $P_0 = 1$ bar, $T_0 = 0°C$, and $\theta \approx 2$ parameterizes the temperature dependence. Note that τ, ϕ, and S_g are all factors between 0 and 1; as air diffuses through vapor in a porous medium it is impeded by the presence of mineral grains (quantified by ϕ), the lack of direct connection between pore spaces (τ), and the presence of liquid water (S_g). One approach to determining D_w is to preserve the symmetry between air and vapor found in free-gas binary diffusion, and define $D_w = D_a$. However, it has been well documented in the soil physics literature that vapor and air do not behave symmetrically, because vapor is condensible, while air is not [e.g., Walker et al., 1981; Jury and Letey, 1979]. Diffusing water vapor will not necessarily be blocked by islands of liquid water held in small pores and throats; it may condense at the higher pressure end of a liquid island, evaporate at the lower pressure end, and continue diffusing. This enhanced diffusion due to pore-level phase-change effects has been modeled successfully by using

$$D_w = \beta D_{va}^0 \frac{P_0}{P}\left[\frac{T+273.15}{273.15}\right]^\theta \tag{19}$$

with β a constant of order one [Jury and Letey, 1979]. A more detailed description of pore-level phase-change effects is given in Tsang and Pruess [1990] and references therein. It is not known at present whether this enhancement of vapor diffusion occurs in deeper consolidated geologic media as well as in soils.

Figure 11 shows the results for a problem that uses $\beta = 1$ in the vapor diffusion term, but is otherwise identical to the with-air problem of Figure 1, with parameters as given in Table 1. The Figure 1 problem uses $\tau = 0.5$ and $\phi = 0.1$. With S_g varying between 0.2 and 1, the $\tau\phi S_g$ group ranges from 0.01 to 0.05. With vapor diffusion away from the heat source enhanced by a factor of up to 100, the counter-flow region is greatly extended (compare Figures 1b and 11b). The diffused vapor condenses over an extended range ($-8.3 < z < -6.8$), causing a long, gradually weakening heat pipe, with smoother variations in fluid flow (Figures 1b and 11b), temperature, and saturation (Figures 1a and 11a) than with $D_w = D_a$. Figure 12 shows the advective and diffusive contributions to gas-phase flows for the $\beta = 1$ case, clearly illustrating that the heat pipe extension is due to diffusion rather than advection. Without the enhanced vapor diffusion, Q^w_{g-diff} would be equal in magnitude and opposite in sign to Q^a_{g-diff}, and would in fact coincide with the Q^a_{g-adv} curve shown. Note that at this expanded scale, a diffusive/advective air counter-flow is visible, but very small; the overall air flow, $Q^a_{g-adv} + Q^a_{g-diff}$, is even smaller.

10. Knudsen Diffusion Using the Klinkenberg *b* Factor

The use of Darcy's law for gas-phase flow implicitly assumes that there are many more collisions among gas molecules than between gas molecules and pore walls. For low pressures or very small pore spaces this may not be a good approximation, and gas flow actually may be greater than predicted by Darcy's law, a phenomenon known as Knudsen diffusion. Laboratory measurements have shown that a simple modification to Darcy's law can predict gas-phase flow under a wide range of conditions. The intrinsic permeability k appearing in the gas-phase mobility $K_g = k k_{rg} \rho_g / \mu_g$ in Equations (A8) and (A9) is replaced by

$$k\left[1 + \frac{b}{P}\right] \tag{20}$$

where b is a constant property of the medium [Klinkenberg, 1941]. Figure 13 shows the results for a problem which uses $b = 7.6$ bars, a value determined in gas-flow experiments on a sample of Yucca Mountain tuff by Reda [1987]. Other parameters are identical to the with-air

problem of Figure 1 (Table 1). For ambient pressures on the order of 1 bar, this value of b causes an increase in effective gas-phase permeability of nearly an order of magnitude, so it is not surprising that the pressure decrease over the length of the heat pipe is much smaller with Knudsen diffusion than without it (compare Figures 1a and 13a). The fluid counter-flow rates are also larger, and more constant than before (Figures 1b and 13b), and the temperature is quite uniform over the length of the heat pipe (Figures 1a and 13a), indicating that nearly all the heat transfer is convective.

The effect of Knudsen diffusion is qualitatively similar to the effect of fractures in which liquid is immobile (compare Figures 1b and 13b to Figures 4b and 7b). The decreased gas-phase pressure for small z somewhat enhances liquid-vapor counter-flow, but the length of the heat pipe is still limited by the liquid-phase mobility. When both gas-phase and liquid-phase mobility are enhanced, as when intrinsic permeability is increased [Doughty and Pruess, 1990, Figures 9 and 10] or fractures in which liquid is mobile are present (Figure 10), the counter-flow is greatly enhanced, generally leading to longer heat pipes and lower temperatures at the heat source.

11. Summary and Conclusions

The mass and energy transport equations for two-phase fluid and heat flow in one-dimensional radial geometry in a homogeneous permeable medium depend on time t and distance r only through the similarity variable $\eta = r/\sqrt{t}$. If initial and boundary conditions can be written as functions of η, then the problem is reduced from a set of partial differential equations to a set of ordinary differential equations. A practically important case for which this is possible is a constant-rate line source at $r = 0$ and uniform initial conditions. These boundary conditions give rise to a two-point boundary value problem which can be solved with an iterative integration scheme. We have applied the similarity variable concept to a problem with a linear heat source emplaced in a partially saturated permeable medium, and have discussed the effect of various parameters in the context of the proposed nuclear waste repository at Yucca Mountain, Nevada, although the solution is certainly not limited to this particular application. The similarity solution has been successfully verified by comparison with numerical finite-difference calculations.

One of the strengths of the similarity variable approach is the ability to study the effect of various transport parameters individually, in a simple geometry. Through this exercise one

develops a knowledge of basic physical processes, which will be valuable when doing more complicated numerical calculations with realistic geometric detail. The examples in the present paper have illustrated the following effects. The presence of air shortens the convective heat-pipe region, thus increasing the temperature at the heat source. A nonzero value for residual liquid saturation has little impact, due to the form of the relative permeability curves typically used to represent geological media. Vapor pressure lowering extends the two-phase region toward the heat source, and makes the onset of counter-flow gradual rather than abrupt. A fractured/porous medium facilitates heat-pipe development compared to a porous medium, but the counter-flow is likely to be small unless liquid is mobile in the fractures. Enhanced vapor diffusion due to pore-level phase-change effects alters the character of the counter-flow region, creating a gradually weakening heat pipe, with less sharp temperature and saturation profiles. Knudsen diffusion fosters heat-pipe development somewhat, but its effect is limited as it only enhances gas-phase flow.

The development of the similarity solution has proceeded in stages. The original version considered only one mass component (water), neglected vapor pressure lowering, and required residual liquid saturation S_{lr} to be zero [Doughty and Pruess, 1990]. It is interesting to note that as more physical realism has been incorporated, some conceptual and numerical problems have been eliminated. For example, for no-air problems, as temperature decreases below the saturation temperature, a purely liquid phase evolves which has an extremely small compressibility. This requires that small integration steps be used, and since pressure signals propagate long distances, a longer integration interval is needed as well. Furthermore, the phase transition from two-phase to single phase requires some special considerations as the primary variable switches from saturation to temperature. With air present, two-phase conditions persist as the temperature drops below the saturation temperature, eliminating these difficulties. When vapor pressure lowering is included, there is no need to distinguish between $S_l < S_{lr}$ and $S_l > S_{lr}$, simplifying the conceptual development of the solution. Additionally, the sharp kink in the saturation profile at S_{lr} for the no-vapor-pressure-lowering case ($dS_l/dz = 0$ for $S_l < S_{lr}$; $dS_l/dz \simeq \infty$ for $S_l > S_{lr}$) becomes a smooth transition when vapor pressure lowering is included, greatly easing step-size requirements for the numerical integration. Formation of a single-phase gas region near the heat source may be suppressed if vapor pressure lowering is strong enough, eliminating the need for any phase transitions or primary variable switching.

The similarity solution results presented here were all calculated using the computer program SIMSOL, which has been fully documented in a laboratory report [Doughty, 1991]. Plans for future work include allowing the inner boundary condition to represent either a heat source or sink, and/or a mass source or sink. This will greatly enhance the applicability of the similarity solution to practical problems, and require only minimal changes to the code. An interesting possible enhancement would be the inclusion of yet another mass component. Components with practical applications include non-condensible gases, (e.g., CO_2), conservative tracers, or volatile organic solvents (such as TCE). Non-aqueous phase liquids (e.g., hydrocarbon compounds) could also be treated by generalyzing the two-phase equilibrium conditions to three phases.

Acknowledgement

The careful review of this work by R. Falta and M. O'Sullivan is greatly appreciated. This work was carried out under U.S. Department of Energy Contract No. DE-AC03-76SF00098, through the Yucca Mountain Project, Sandia National Laboratories, under Document No. SNL 54-1064; numerical computations were supported by the Director, Office of Energy Research, Office of Basic Energy Sciences, Engineering and Geosciences Division, U.S. Department of Energy.

References

Corey, A. T., 1954. The interrelation between gas and oil relative permeabilities. *Producers Monthly* **Nov.**, 38-41.

Doughty, C., 1991. SIMSOL Users Guide. Report LBL-28384, Lawrence Berkeley Lab., Berkeley, Calif.

Doughty, C. and Pruess, K., 1990. A similarity solution for two-phase fluid and heat flow near high-level nuclear waste packages emplaced in porous media. *Int. J. Heat Mass Transfer* **33**(6), 1205-1222.

Firoozabadi, A. and Hauge, J., 1990. Capillary pressure in fractured porous media. *J. Petroleum Technology* **June**, 784-791.

Grant, M. A., 1979. Quasi-analytic solutions for two-phase flow near a discharging well. Report 86, Applied Mathematics Division, Dept. of Scientific and Industrial Research, Wellington, New Zealand.

Hirschfelder, J. O., Curtiss, C. F., and Bird, R. B., 1954. *Molecular Theory of Gases and Liquids*. John Wiley and Sons, New York.

International Formulation Committee, 1967. *A formulation of the thermodynamic properties of ordinary water substance*. IFC Secretariat, Düsseldorf, Germany.

Jennings, J. D. and Udell, K. S., 1985. The heat pipe effect in heterogeneous porous media. In *Proc. 23rd ASME/AIChe National Heat Transfer Conf.*, HTD Vol. 46, *Heat transfer in porous media and particulate flows*, American Society of Mechanical Engineers.

Jury, W. A. and Letey, J., Jr., 1979. Water vapor movement in soil: reconciliation of theory and experiment. *Soil Sci. Soc. Am. J.* **43**(5), 823-827.

Klinkenberg, L. J., 1941. The permeability of porous media to liquids and gases. *Drilling and Production Practice*, American Petroleum Inst., 200-213.

Loomis, A. G., 1928. Solubilities of gases in water. In *International Critical Tables*, E. W. Washburn, ed., McGraw HIll, New York, Vol. III, pp. 255-257.

Narasimhan, T. N. and Witherspoon, P. A., 1976. An integrated finite-difference method for analyzing fluid flow in porous media. *Water Resour. Res.* **12**(1), 57-64.

O'Sullivan, M., J., 1981. A similarity method for geothermal well test analysis. *Water Resour. Res.* **17**(2), 390-398.

Press, W. H., Flannery, B. P., Teukolsky, S. A., and Vetterling, W. T., 1986. *Numerical Recipes: The art of scientific computing*. Cambridge University Press, New Rochelle, New York, Ch. 16.

Pruess, K., 1987. TOUGH user's guide. Report NUREG/CR-4645, Nuclear Regulatory Commission, Washington, D.C. (Also avail. as Lawrence Berkeley Laboratory Report LBL-

20700.)

Pruess, K., 1990. TOUGH2–A general-purpose numerical simulator for multiphase fluid and heat flow. Report LBL-29400, Lawrence Berkeley Lab., Berkeley, Calif.

Pruess, K. and Tsang, Y. W., 1990. On two-phase relative permeability and capillary pressure of rough-walled fractures. *Water Resour. Res.* **26**(9),1915-1926.

Pruess, K., Tsang, Y. W., and Wang, J. S. Y., 1990a. On thermohydrological conditions near high-level nuclear wastes emplaced in partially saturated fractured tuff. Part 1. Simulation studies with explicit consideration of fracture effects. *Water Resour. Res.* **26**(6), 1235-1248.

Pruess, K., Wang, J. S. Y., and Tsang, Y. W., 1990b. On thermohydrological conditions near high-level nuclear wastes emplaced in partially saturated fractured tuff. Part 2. Effective continuum approximation. *Water Resour. Res.* **26**(6), 1249-1261.

Reda, D. C., 1987. Slip-flow experiments in welded tuff: the Knudsen diffusion problem. In *Coupled processes associated with nuclear waste repositories*, C.-F. Tsang, ed., Academic Press, Orlando, Florida, pp. 485-494.

Rulon, J., Bodvarsson, G. S., Montazer, P., 1986. Preliminary numerical simulations of groundwater flow in the unsaturated zone, Yucca Mountain, Nevada. Report LBL-20553, Lawrence Berkeley Lab., Berkeley, Calif.

Somerton, W. H., Keese, J. A., and Chu, S. L., 1973. Thermal behavior of unconsolidated oil sands. Paper SPE-4506, 48th Annual Fall Meeting of the Society of Petroleum Engineers, Las Vegas, Nevada.

Somerton, W. H., El-Shaarani, A. H., and Mobarak, S. M., 1974. High temperature behavior of rocks associated with geothermal type reservoirs. Paper SPE-4897, 44th Annual California Regional Meeting of the Society of Petroleum Engineers, San Francisco, Calif.

Tsang, Y. W. and Pruess, K., 1990. Further modeling of gas movement and moisture migration at Yucca Mountain, Nevada. Report LBL-29127, Lawrence Berkeley Lab., Berkeley, Calif.

van Genuchten, M. Th., 1980. A closed-form equation for predicting the hydraulic conductivity of unsaturated soils. *Soil Sci. Soc. Am. J.* **44**, 892-898.

Vargaftik, N. B., 1975. *Tables on the thermophysical properties of liquids and gases*, 2nd edition. John Wiley and Sons, New York.

Verma, A. K., Pruess, K., Tsang, C.-F., and Witherspoon, P. A., 1985. A study of two-phase concurrent flow of steam and water in an unconsolidated porous medium. In *Proc. 23rd ASME/AIChe National Heat Transfer Conf.*, HTD Vol. 46, *Heat transfer in porous media and particulate flows*, pp. 135-143. American Society of Mechanical Engineers.

Walker, W. R., Sabey, J. D., and Hampton, D. R., 1981. Studies of heat transfer and water migration in soils, Final Report. Department of Agricultural and Chemical Engineering,

Colorado State University, Fort Collins, CO.

Wang, J. S. Y. and Narasimhan, T. N., 1985. Hydrologic mechanisms governing fluid flow in a partially saturated, fractured, porous medium. *Water Resour. Res.* **21**(12), 1861-1874.

Appendix A: Governing Equations and Thermophysical Properties

Conservation equations in radial geometry

$$\frac{\partial M_m}{\partial t} + \frac{1}{2\pi r}\frac{\partial Q_m}{\partial r} = 0 \qquad \text{for } m = w, a, e \tag{A1}$$

Accumulation terms

$$M_m = \phi(S_l \rho_l X_l^m + S_g \rho_g X_g^m) \qquad \text{for } m = w, a \tag{A2}$$

$$M_e = (1-\phi)\rho_s c_s T + \phi(S_l \rho_l u_l + S_g \rho_g u_g), \tag{A3}$$

Flux terms

$$Q_m = Q_l^m + Q_g^m$$

$$= -2\pi r\left[\left[\frac{kk_{rl}\rho_l X_l^m}{\mu_l}\frac{\partial P_l}{\partial r}\right] + \left[\frac{kk_{rg}\rho_g X_g^m}{\mu_g}\frac{\partial P_g}{\partial r} + D_m \rho_g \frac{\partial X_g^m}{\partial r}\right]\right] \qquad \text{for } m = w, a \tag{A4}$$

$$Q_e = \sum_{\substack{j=l,g \\ m=w,a}} h_j^m Q_j^m - \kappa 2\pi r \frac{\partial T}{\partial r}, \tag{A5}$$

Closure conditions

$$X_l^m + X_g^m = 1 \qquad \text{for } m = w, a \tag{A6}$$

$$S_l + S_g = 1$$

$$P_g = P_v + P_a$$

$$P_c = P_l - P_g$$

With the substitution $z = \ln(\eta) = \ln(r/\sqrt{t})$, the partial differential equations become ordinary differential equations. The chain rule is then used to express the governing equations in terms of derivatives of the primary variables. For example, for two-phase conditions the accumulation terms become

$$\frac{1}{2\pi}\frac{dQ_m}{dz} = \frac{e^{2z}}{2}\left[\frac{\partial M_m}{\partial P_g}\frac{dP_g}{dz} + \frac{\partial M_m}{\partial S_g}\frac{dS_g}{dz} + \frac{\partial M_m}{\partial P_a}\frac{dP_a}{dz}\right] \qquad \text{for } m = w, a, e. \tag{A7}$$

The flux terms become

$$\frac{Q_m}{2\pi} = -\left[K_l X_l^m\left[1 + \frac{\partial P_c}{\partial P_g}\right] + K_g X_g^m + D_m \rho_g \frac{\partial X_g^m}{\partial P_g}\right]\frac{dP_g}{dz} - \left[K_l X_l^m \frac{\partial P_c}{\partial S_g}\right]\frac{dS_g}{dz}$$

$$- \left[K_l X_l^m \frac{\partial P_c}{\partial P_a} + D_m \rho_g \frac{\partial X_g^m}{\partial P_a} \right] \frac{dP_a}{dz} \qquad \text{for } m = w, a \tag{A8}$$

$$\frac{Q_e}{2\pi} = - \left[\sum_{m=w,a} \left[h_l^m K_l X_l^m \left[1 + \frac{\partial P_c}{\partial P_g} \right] + h_g^m K_g X_g^m \right] + (h_g^a D_a - h_g^w D_w) \rho_g \frac{\partial X_g^a}{\partial P_g} + \kappa \frac{\partial T}{\partial P_g} \right] \frac{dP_g}{dz}$$

$$- \left[\sum_{m=w,a} \left[h_l^m K_l X_l^m \right] \frac{\partial P_c}{\partial S_g} + \kappa \frac{\partial T}{\partial S_g} \right] \frac{dS_g}{dz}.$$

$$- \left[\sum_{m=w,a} \left[h_l^m K_l X_l^m \right] \frac{\partial P_c}{\partial P_a} + (h_g^a D_a - h_g^w D_w) \rho_g \frac{\partial X_g^a}{\partial P_a} + \kappa \frac{\partial T}{\partial P_a} \right] \frac{dP_a}{dz}. \tag{A9}$$

Equations (A8) and (A9) are solved for dP_g/dz, dS_g/dz, and dP_a/dz, which are then substituted into Equation (A7) to determine dQ_w/dz, dQ_a/dz, and dQ_e/dz. This produces a set of six coupled first-order ODEs in the form required for numerical integration.

The constitutive relationships used to define the thermodynamic parameters in terms of the primary variables are taken from the numerical simulator TOUGH [Pruess, 1987, 1990].

Steam tables, given by the International Formulation Committee [IFC, 1967] provide closed-form expressions for ρ, u, h, and μ, as functions of P and T for the water component, as well as the surface tension of water (used in P_c), and vapor pressure P_{sat} as functions of T. Vapor pressure lowering is determined using the Kelvin equation as described in Section 7. Air is treated as an ideal gas, with Henry's law to determine the solubility of air in liquid water

$$P_a = K_H X_l^a \cdot \frac{M_{H_2O}}{M_{air}} \tag{A10}$$

where K_H is Henry's constant, and M_{H_2O} and M_{air} are the molecular weights of water and air, respectively. Henry's constant is temperature-dependent; however, because air solubility in water is small we neglect this temperature dependence. The value $K_H = 10^{10}$ Pa used here is accurate to within 10% in the temperature range from 40°C to 100°C [Loomis, 1928]. Viscosity of the vapor-air mixture making up the gas phase is computed from a formulation given by Hirschfelder et al. [1954], but using steam-table values for vapor viscosity instead of approximations from kinetic gas theory.

Gas-phase permeability can depend on pressure through the Klinkenberg [1941] relationship $k_g = k_l \cdot (1 + b/P)$. Relative permeabilities k_{rl} and k_{rg} and capillary pressure P_c are functions of liquid and gas saturation S_l and S_g; an example is shown in Table 1. "Double

hump'' curves (Figure 7b) can be used for approximate representation of flow in fractured-porous media. Vapor diffusivity D_w can be enhanced to represent pore-level phase change effects (Section 9). Thermal conductivity κ may vary with liquid saturation, as determined by Somerton et al. [1973, 1974] from laboratory experiments

$$\kappa = \kappa_g + \sqrt{S_l}(\kappa_l - \kappa_g), \tag{A11}$$

where κ_g and κ_l are the values of thermal conductivity for dry and liquid-saturated rock, respectively.

Porosity may depend on pressure and temperature:

$$\phi = \phi_0 \exp\left[\beta_s (P - P_0) + \alpha_s (T - T_0)\right], \tag{A12}$$

where β_s and α_s are constant rock compressibility and rock expansivity, respectively, and ϕ_0 is the value of porosity for $P_g = P_0$ and $T = T_0$.

Rock density ρ_s and rock specific heat c_s are assumed to be constants.

Appendix B: Modification of the van Genuchten Capillary Pressure Function for Small Values of Liquid Saturation

The van Genuchten [1980] formulation for capillary pressure as a function of liquid saturation is given by

$$P_c(S_l) = -P_0\left[(S^*)^{-1/\lambda} - 1\right]^{1-\lambda} \tag{B1}$$

where $S^* = (S_l - S_{lr})/(S_{ls} - S_{lr})$, S_{lr} and S_{ls} are the saturations at which liquid is fully immobile and fully mobile, respectively, and P_0 and λ are parameters used to fit the functional form to observed data. The parameter λ takes a value between 0 and 1. Equation (B1) has the properties that S^* must be non-negative, and that as $S^* \to 0$, $P_c \to -\infty$. Infinite quantities are not well-suited to computer representation, and if $S_l < S_{lr}$, S^* will be negative, so Equation (B1) has been modified for small values of liquid saturation. A parameter P_{max} is defined as the maximum strength of capillary pressure to be calculated with Equation (B1); Equation (B1) is then inverted to determine S_p, the value of S^* that gives $P_c = P_{max}$. The range of application of Equation (B1) is thus restricted to $S^* > S_p$ and new bounded functions are introduced for smaller values of S^*.

$$P_{c1}(S_l) = -P_0\left[(S^*)^{-1/\lambda} - 1\right]^{1-\lambda} \qquad S_p < S^* < 1 \tag{B2}$$

$$P_{c2}(S_l) = -P_{max}\exp\left[\frac{(1-\lambda)(1-S^*/S_p)}{\lambda(1-S_p^{1/\lambda})}\right] \qquad 0 < S^* < S_p \tag{B3}$$

$$P_{c3}(S_l) = -P_{max}\exp\left[\frac{(1-\lambda)}{\lambda(1-S_p^{1/\lambda})}\right]\cdot\left[1 - \frac{(1-\lambda)S^*/S_p}{\lambda(1-S_p^{1/\lambda})}\right] \qquad S^* < 0 \tag{B4}$$

Together, Equations (B2), (B3)†, and (B4) provide a continuous, differentiable capillary pressure function, which remains finite as $S^* \to 0$ and below. By choosing a large value of P_{max}, S_p is small and the van Genuchten capillary pressure function is used for most of the range of S_l. For the similarity solution it is also necessary that the capillary pressure have a nonzero derivative throughout the two-phase zone; this requires that $S_{ls} = 1$ in the definition of S^*.

†Equation (B3) was originally developed for numerical simulations of groundwater flow at Yucca Mountain [Rulon et al., 1986].

Table 1. Parameters for problems illustrated in Figures 1, 2, 3, 11, 12, and 13. Parameters are modified from typical Yucca Mountain values, see text.

Boundary and Initial Conditions	
$z = \ln(\eta) = \ln(r/\sqrt{t}) = -\infty$	$Q_{e0} = 667$ W/m*
	$Q_{w0} = 0$
	$Q_{a0} = 0$†
$z = \ln(\eta) = \ln(r/\sqrt{t}) = +\infty$	$P_0 = 1$ bar
	$T_0 = 18°C$
	$S_{l0} = 0.8$†
Material Properties	
$k = 20\times10^{-15}$ m^2	$\kappa = 2$ W/m K
$\phi = 0.10$	$\tau = 0.5$
$\rho_s = 2550$ kg/m^3	$D_{va}^0 = 2.6\times10^{-5}$ m^2/s
$c_s = 800$ J/kg K	$\theta = 0$
Characteristic Curves‡	
$k_{rl}(S_l) = \sqrt{S^*}\left[1-(1-(S^*)^{1/\lambda})^{\lambda}\right]^2$	$S_{lr} = 9.6\times10^{-4}$
$k_{rg}(S_l) = 1-k_{rl}$	$\lambda = 0.45$
$P_c(S_l) = -P_0\left[(S^*)^{-1/\lambda}-1\right]^{1-\lambda}$	$P_0 = 0.125$ bars
$S^* = (S_l-S_{lr})/(1-S_{lr})$	$P_{max} = 5000$ bars§

*This thermal power corresponds to high-level nuclear wastes approximately 10 years old.

†In Figure 1, used for with-air problem only.

‡Functional forms of van Genuchten [1980]; P_c has been modified slightly, see Appendix B.

§For $S^* \rightarrow 0$, $P_c(S_l)$ would go to $-\infty$, but is limited to the order of $-P_{max}$ (see Appendix B).

Table 2. Parameters for problems illustrated in Figures 5, 8, 9, and 10. Parameters are typical of Yucca Mountain values [Tsang and Pruess, 1990].

Boundary and Initial Conditions	
$z=\ln(\eta)=\ln(r/\sqrt{t})=-\infty$	$Q_{e0}=667$ W/m*
	$Q_{w0}=0$
	$Q_{a0}=0$
$z=\ln(\eta)=\ln(r/\sqrt{t})=+\infty$	$P_0=1$ bar
	$T_0=22°C$
	$S_{l0}=0.7$
Material Properties	
$k_m = 1.9\times10^{-18}$ m^2	$\tau = 0.25$
$\phi_m = 0.10$	$D_{va}^0 = 2.14\times10^{-5}$ m^2/s
$\rho_s = 2480$ kg/m^3	$\theta = 2.334$
$c_s = 840$ J/kg K	$k_f = 10^{-11}$ m^2
$\kappa = 1.9$–2.34 W/m K	$\phi_f = 1.0$
	$V_f = 0.0018$†
Characteristic Curves‡	
$k_{rlm}(S_l) = \sqrt{S^*}\left[1-(1-(S^*)^{1/\lambda})^{\lambda}\right]^2$	$S_{lr} = 8.01\times10^{-2}$
$k_{rgm}(S_l) = 1-k_{rl}$	$\lambda = 0.4438$
$P_{cm}(S_l) = -P_0\left[(S^*)^{-1/\lambda}-1\right]^{1-\lambda}$	$P_0 = 17.3$
$S^* = (S_l-S_{lr})/(1-S_{lr})$	$P_{max} = 5000$ bars§

*This thermal power corresponds to high-level nuclear wastes approximately 10 years old.

†$V_f=0$ for Figure 5; $V_f=0.05$ for Figure 9.

‡Functional forms of van Genuchten [1980]; P_{cm} has been modified slightly, see Appendix B. For Figure 5, which shows results for a no-fracture problem ($V_f=0$), these characteristic curves are used directly. For Figures 8, 9, and 10, which show results for fracture/matrix problems, the characteristic curves given here refer to the matrix; Table 4 describes the complete effective-continuum characteristic curves.

§For $S^* \to 0$, $P_c(S_l)$ would go to $-\infty$, but is limited to the order of $-P_{max}$ (see Appendix B).

Table 3. Characteristic curves to use in iterative solution of Equations (11), (12), and (13). $P_{cm}(S_{lm})$ and $P_{cf}(S_{lf})$ are shown in Figure 6. Modified from Pruess et al. [1990a].

$P_{cm}(S_{lm})$	from Table 2	
$P_{cf}(S_{lf})$	$=P_{cm}(0)\,(1-S_{lf}/S_{crit})$	$S_{lf} < S_{crit} - \delta_c$
	$=P_{cm}(0)\dfrac{\delta_c}{S_{crit}}\left[\dfrac{1-S_{lf}}{1-S_{crit}+\delta_c}\right]$	$S_{lf} > S_{crit} - \delta_c$
	with P_{cm} from Table 2, $S_{crit}=0.0099$ or 0.01002, $\delta_c = 10^{-9}$	
$k_{rlm}(S_{lm})$	from Table 2	
$k_{rlf}(S_{lf})$	$=(S_{lf}-S_{lrf})/(1-S_{lrf})$	
	$S_{lrf}=0.01$	

Table 4. Approximate closed-form characteristic curves shown in Figure 7.

Source	Application	Function		
Sequential	Figs. 8, 9, 10	P_c	$= P_{cm}\left[(1-\delta_s)\tilde{S}_l/S_{th}\right]$	$\tilde{S}_l < S_{th}$
Saturation			$= \dfrac{1-\tilde{S}_l}{1-S_{th}} \cdot P_{cm}(1-\delta_s)$	$\tilde{S}_l > S_{th}$
Model		with P_{cm} from Table 2, $\delta_s = 10^{-4}$		
Sequential	Figs. 8, 9	Use $\tilde{k}_{rl}$, $\tilde{k}_{rg}$ from Eq. (13), with		
Saturation		k_{rlm}	$= k_{rlm}(\tilde{S}_l/S_{th})$ from Table 2	$\tilde{S}_l < S_{th}$
Model		k_{rlf}	$= 0$	
		k_{rlm}	$= 1$	$\tilde{S}_l > S_{th}$
		k_{rlf}	$= (\tilde{S}_l - S_{th})/(1-S_{th})$	
Alternate	Fig. 10	$\tilde{k}_{rl}$	$= \hat{k}[(\tilde{S}_l - \hat{S}_{lr})/(S_{th} - \hat{S}_{lr})]^{\hat{\varepsilon}}$	$\tilde{S}_l < S_{th}$
Curve Fit,			$= \hat{k} + (1-\hat{k})(\tilde{S}_l - S_{th})/(1-S_{th})$	$\tilde{S}_l > S_{th}$
$S_{crit} > S_{lrf}$		with $\hat{k} = 0.55\times10^{-4}$, $\hat{\varepsilon}=0.8$, $\hat{S}_{lr} = 0.13$		
		$\tilde{k}_{rg}$	$= 1 - \tilde{k}_{rl}$	

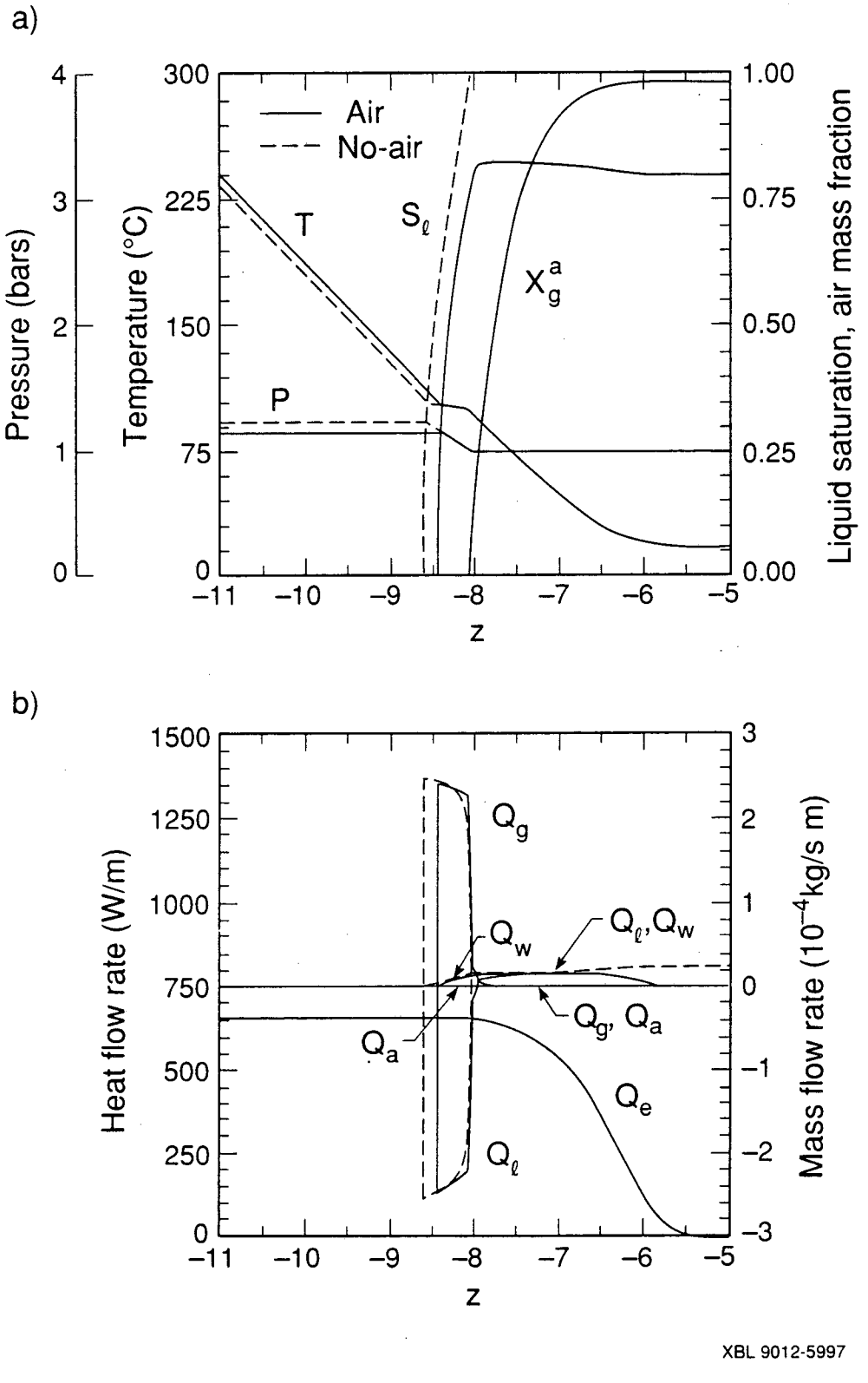

Figure 1. Results of the similarity solution for the with-air and no-air problems described in Table 1.

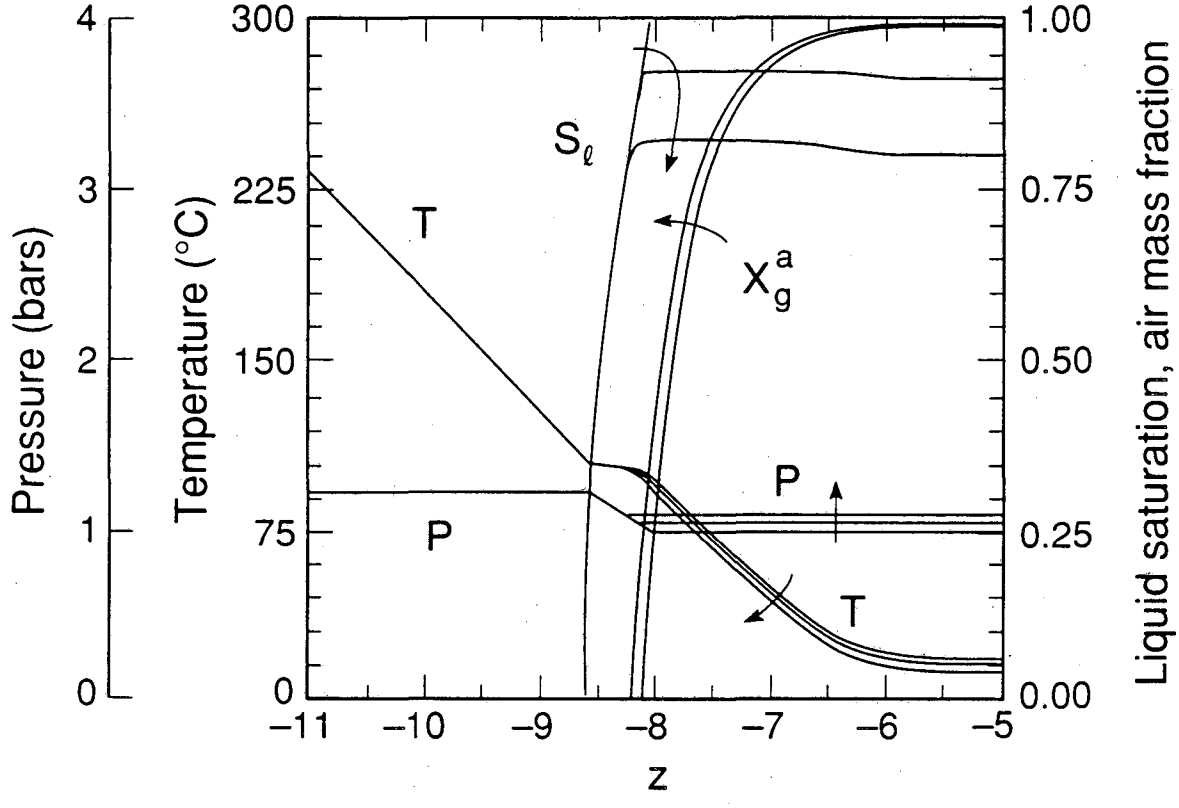

XBL 9012-5998

Figure 2. The effect of increasing the amount of air at z_L on the no-air problem shown in Figure 1 and described in Table 1. The arrows show the direction of change as $P_a(z_L)$ is increased from 0 to 10^{-41} to 10^{-26} bars. For comparison, for the with-air problem of Figure 1, $P_a(z_L) = 10^{-24}$ bars.

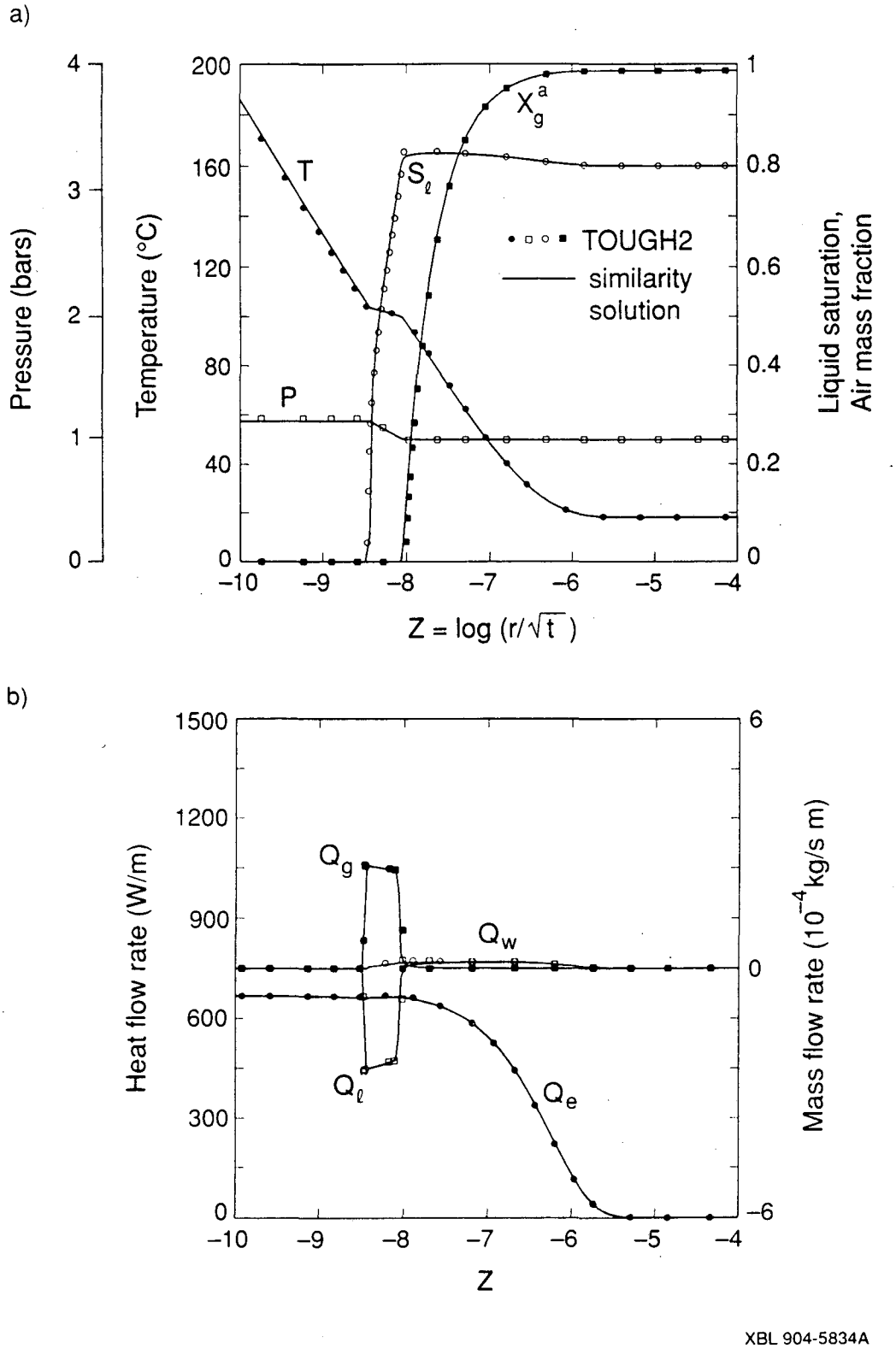

Figure 3. A comparison between results of the similarity solution and the numerical model TOUGH2 for the with-air problem described in Table 1.

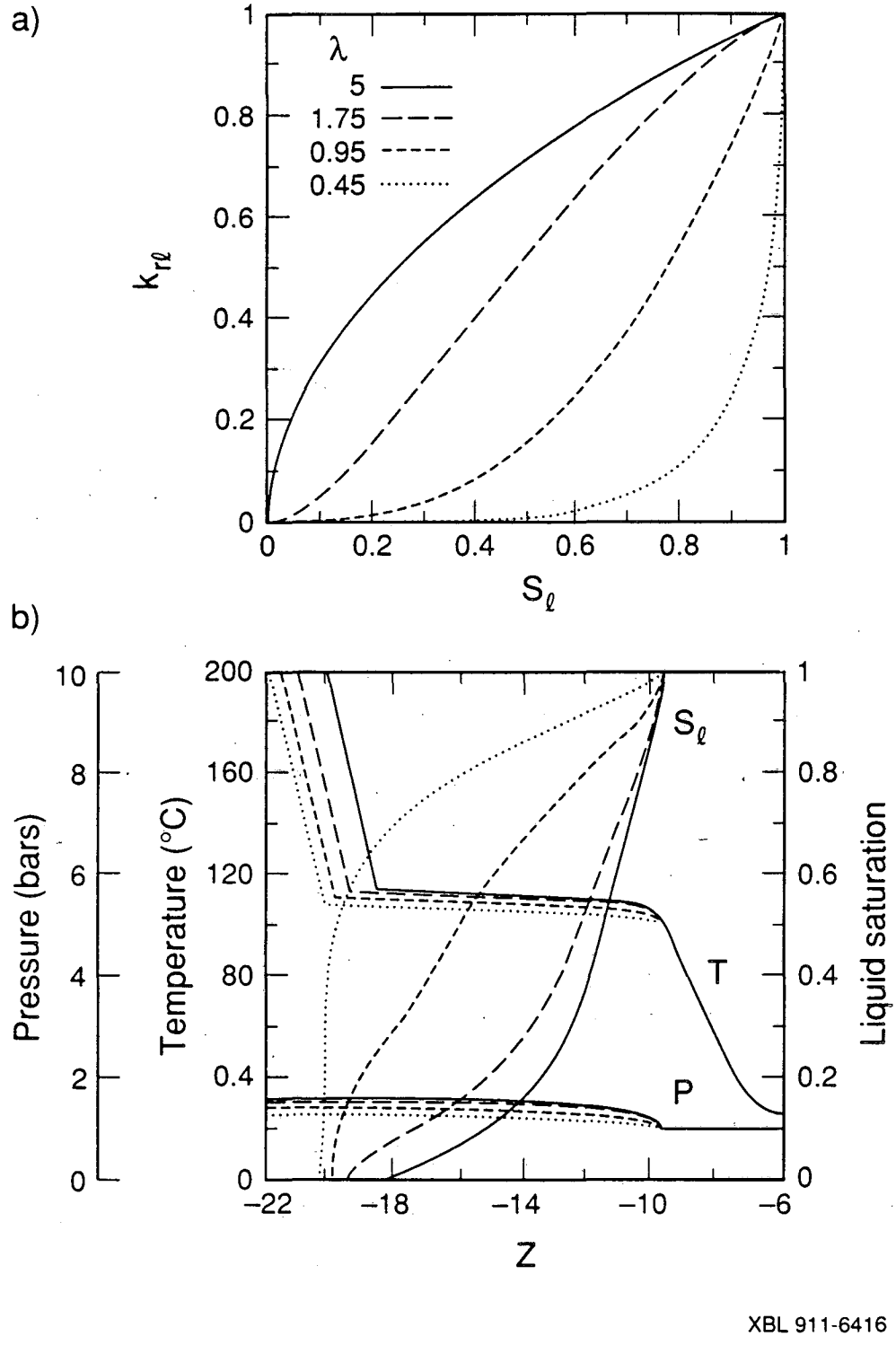

Figure 4. Various liquid relative permeability curves (4a) and the corresponding similarity solution results (4b) for a series of no-air problems. In all cases $k_{rg} = 1 - k_{rl}$, and $S_{lr} = 0$. Other parameters are given in Doughty and Pruess [1990, Table 1].

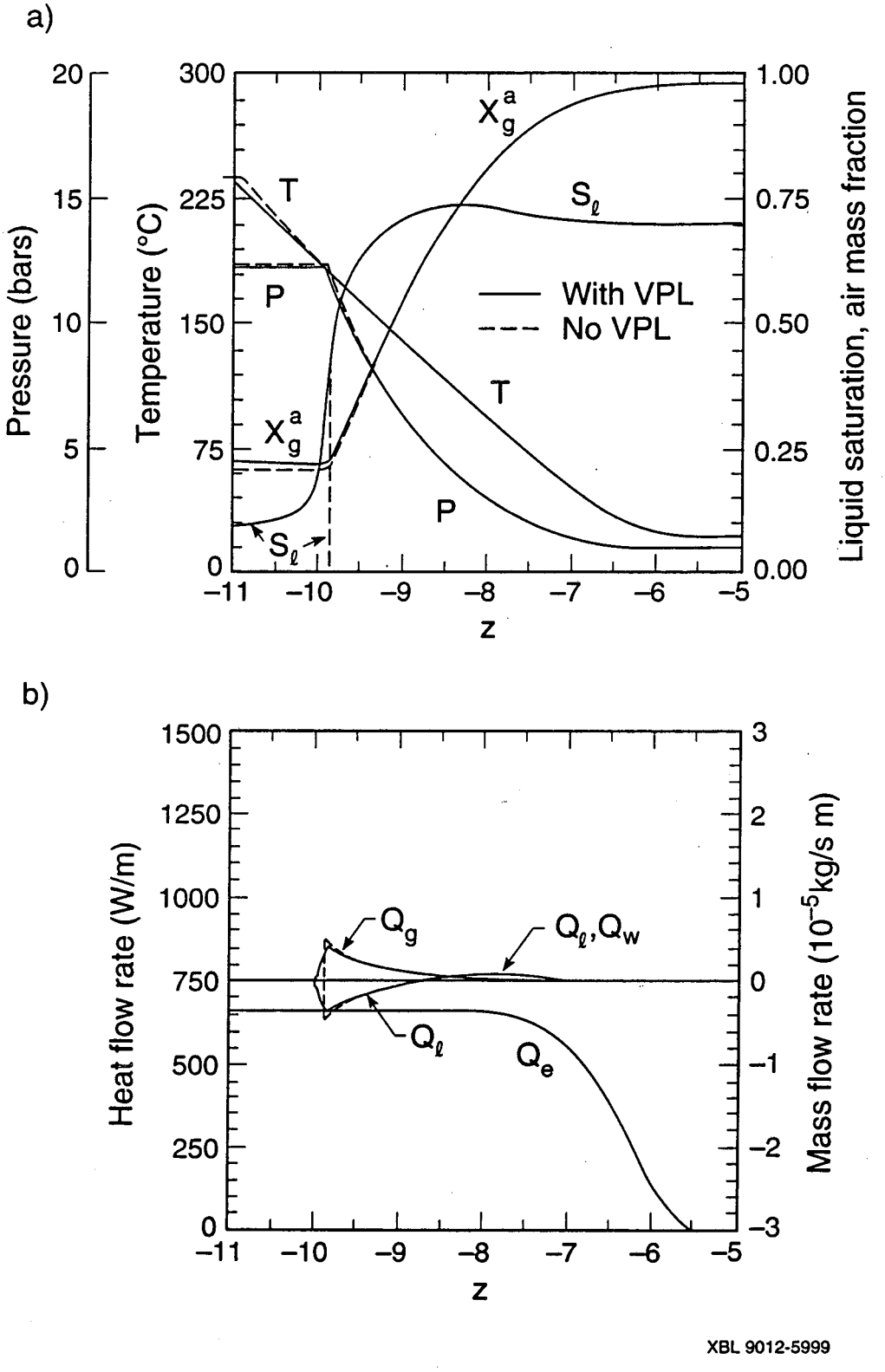

Figure 5. Results of the similarity solution for problems with and without vapor pressure lowering, described in Table 2. Note the change of scale for mass flow rate!

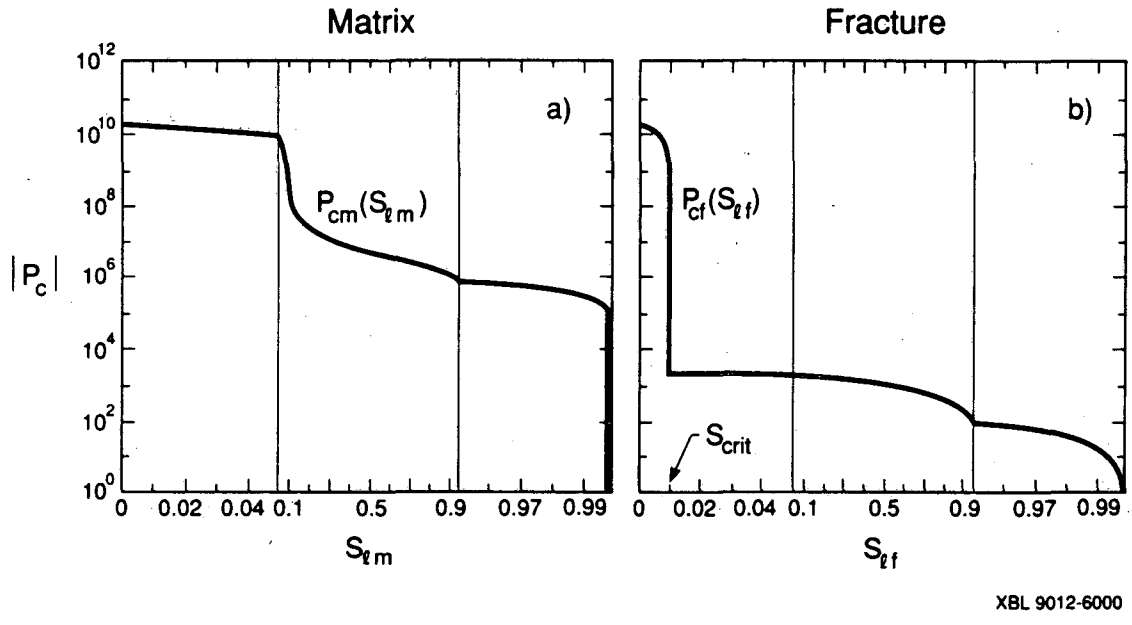

Figure 6. Matrix capillary pressure as a function of matrix liquid saturation, for the functional forms and parameter values given in Table 2 (6a), and fracture capillary pressure as a function of fracture liquid saturation, for the functional forms and parameter values given in Table 3 (6b). Note that the S_l scale is linear, with the saturation ranges 0–0.05 and 0.95–1 expanded to enable more detail to be shown.

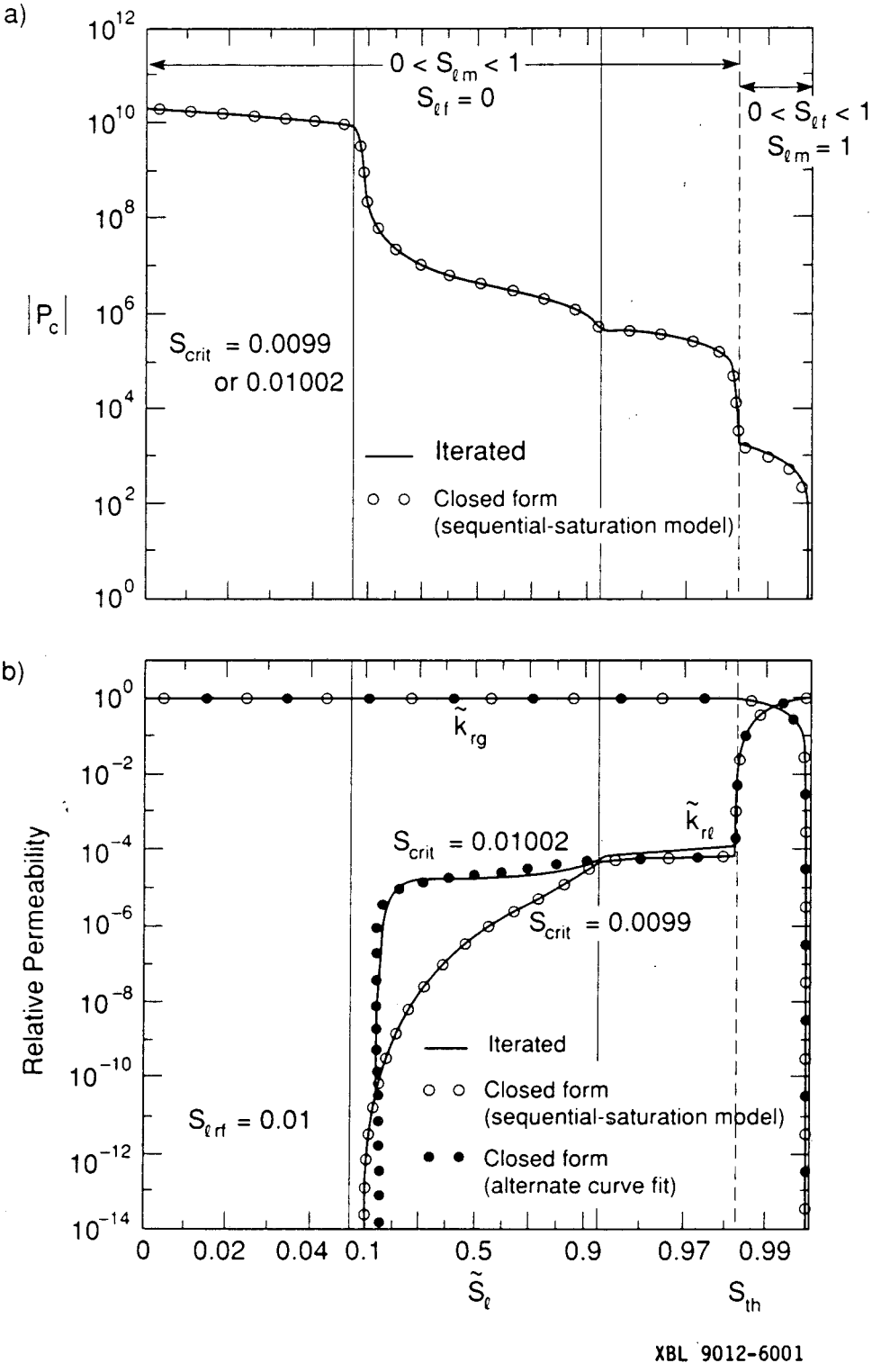

Figure 7. Effective-continuum capillary pressure $P_c(\tilde{S}_l)$ (7a) and relative permeabilities $\tilde{k}_{rl}$ and $\tilde{k}_{rg}$ (7b) obtained with (i) an iterative solution using the functions shown in Figure 6 and given in Table 3, and (ii) the approximate closed-form solutions given in Table 4. Note that the S_l scale is linear, with the saturation ranges 0–0.05 and 0.95–1 expanded to enable more detail to be shown.

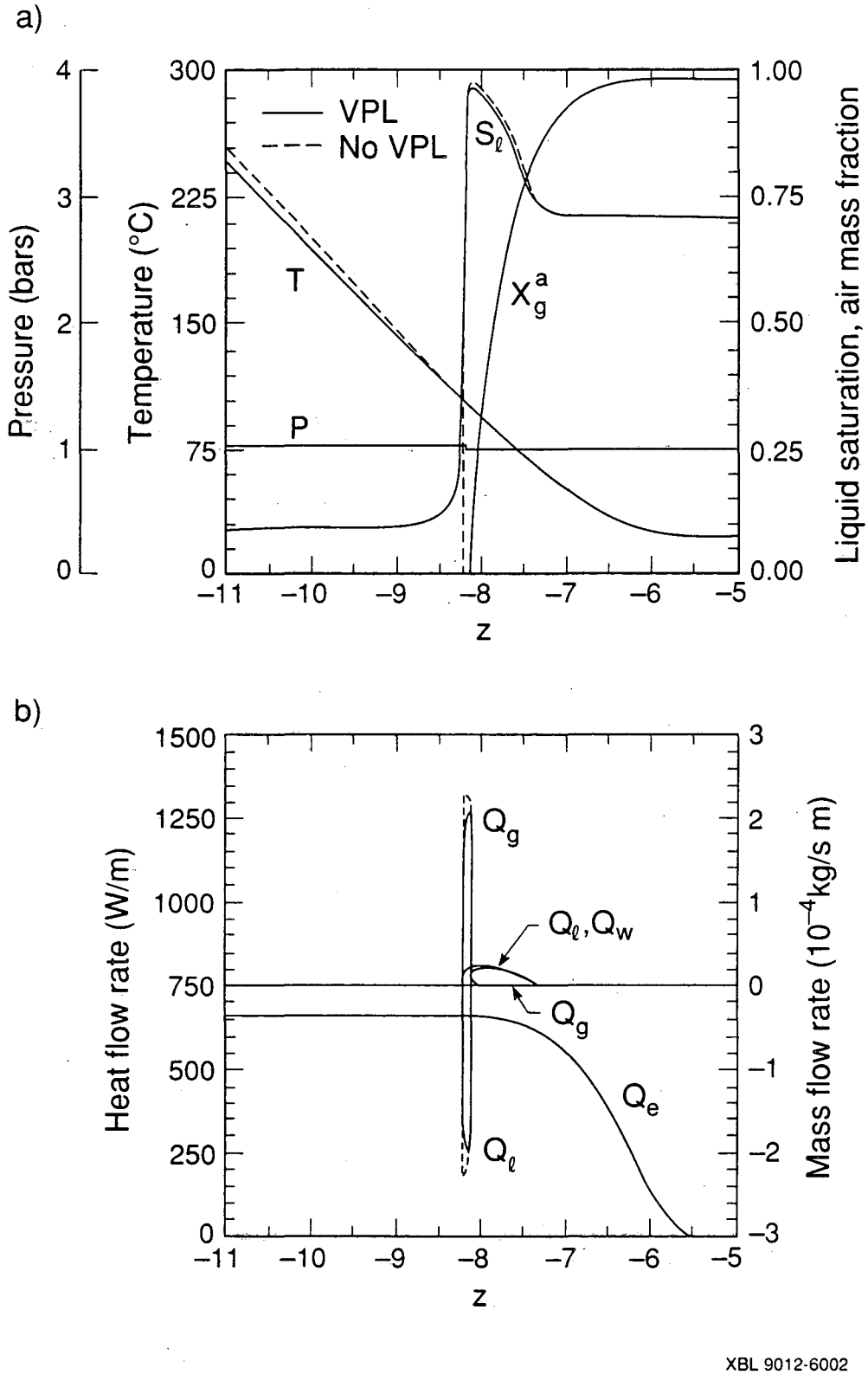

Figure 8. Results of the similarity solution for an effective continuum using the sequential-saturation model, with properties given in Tables 2 and 4. The peak liquid saturation in the halo (0.964) is less than the threshold saturation (S_{lh} =0.982), which is greater than far-field liquid saturation (S_{l0}=0.7). Results without vapor pressure lowering are also shown.

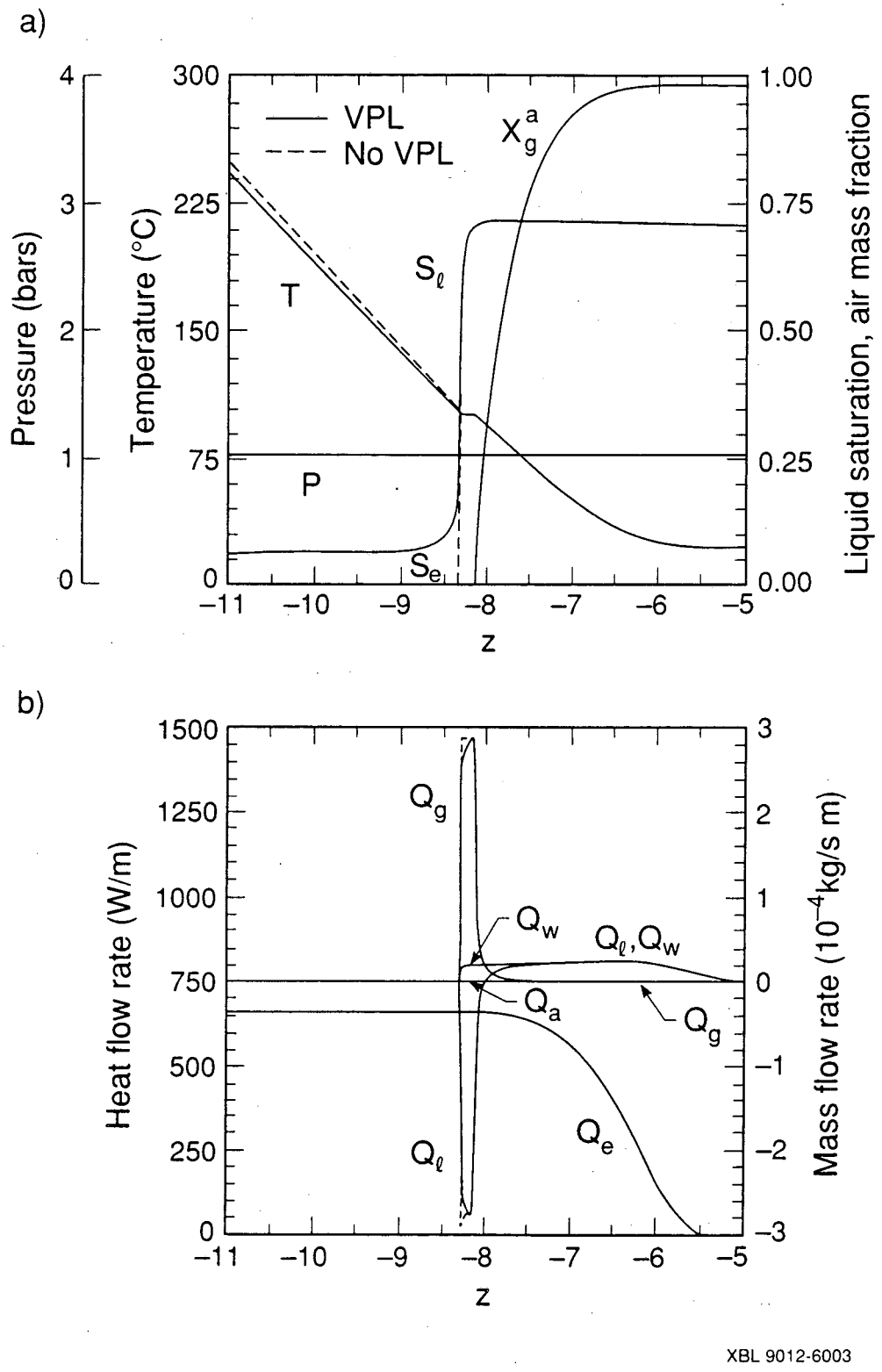

Figure 9. Results of the similarity solution for the same problem as shown in Figure 8, but with the fracture volume increased to $V_f = 0.05$, so that $S_{th} = 0.65$ is less than $S_{l0} = 0.7$. Results without vapor pressure lowering are also shown.

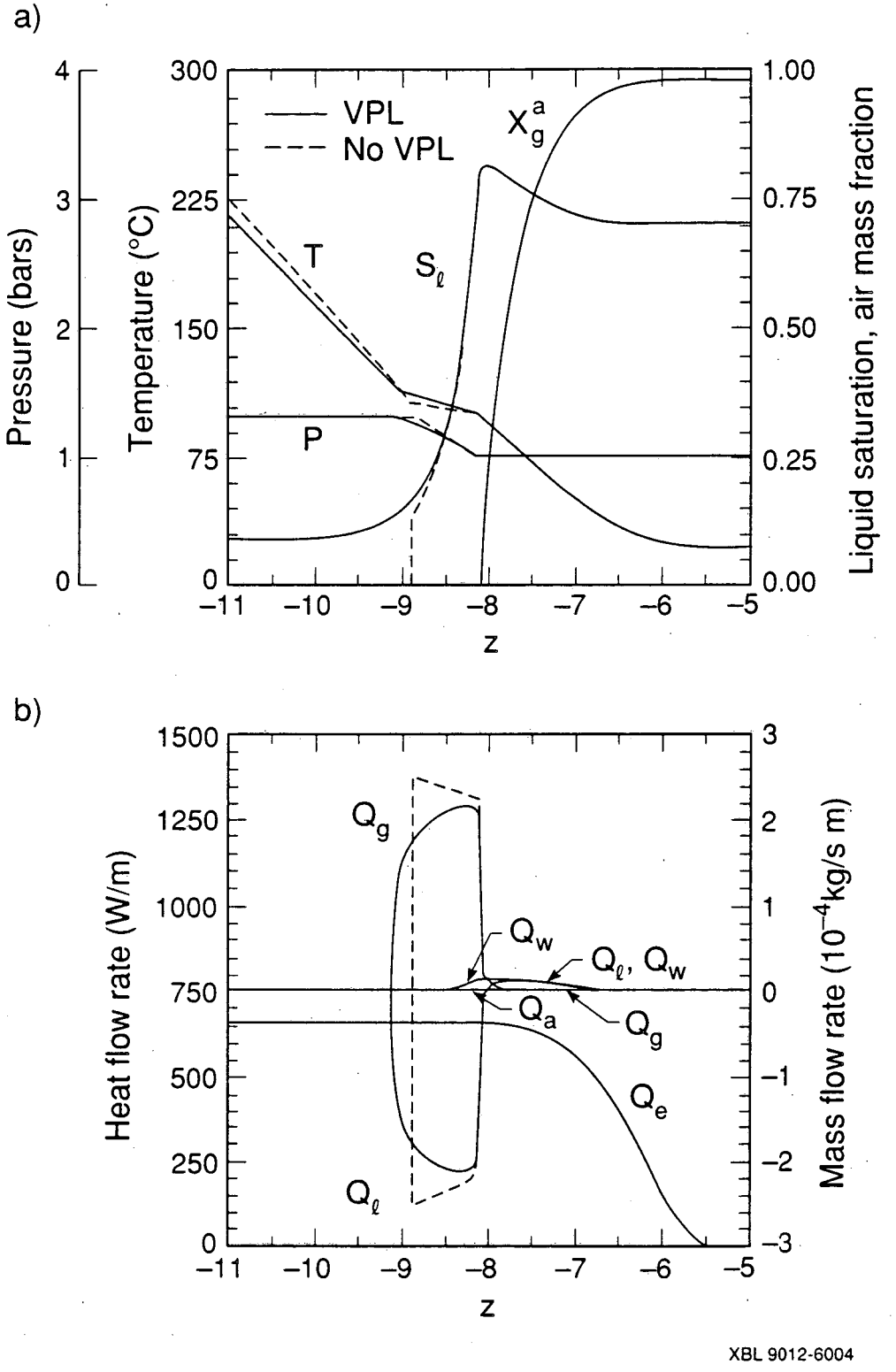

Figure 10. Results of the similarity solution for an effective continuum using the closed-form approximation to the concurrent-saturation relative permeability curves for $S_{criu} > S_{lrf}$, with properties given in Tables 2 and 4. Results without vapor pressure lowering are also shown.

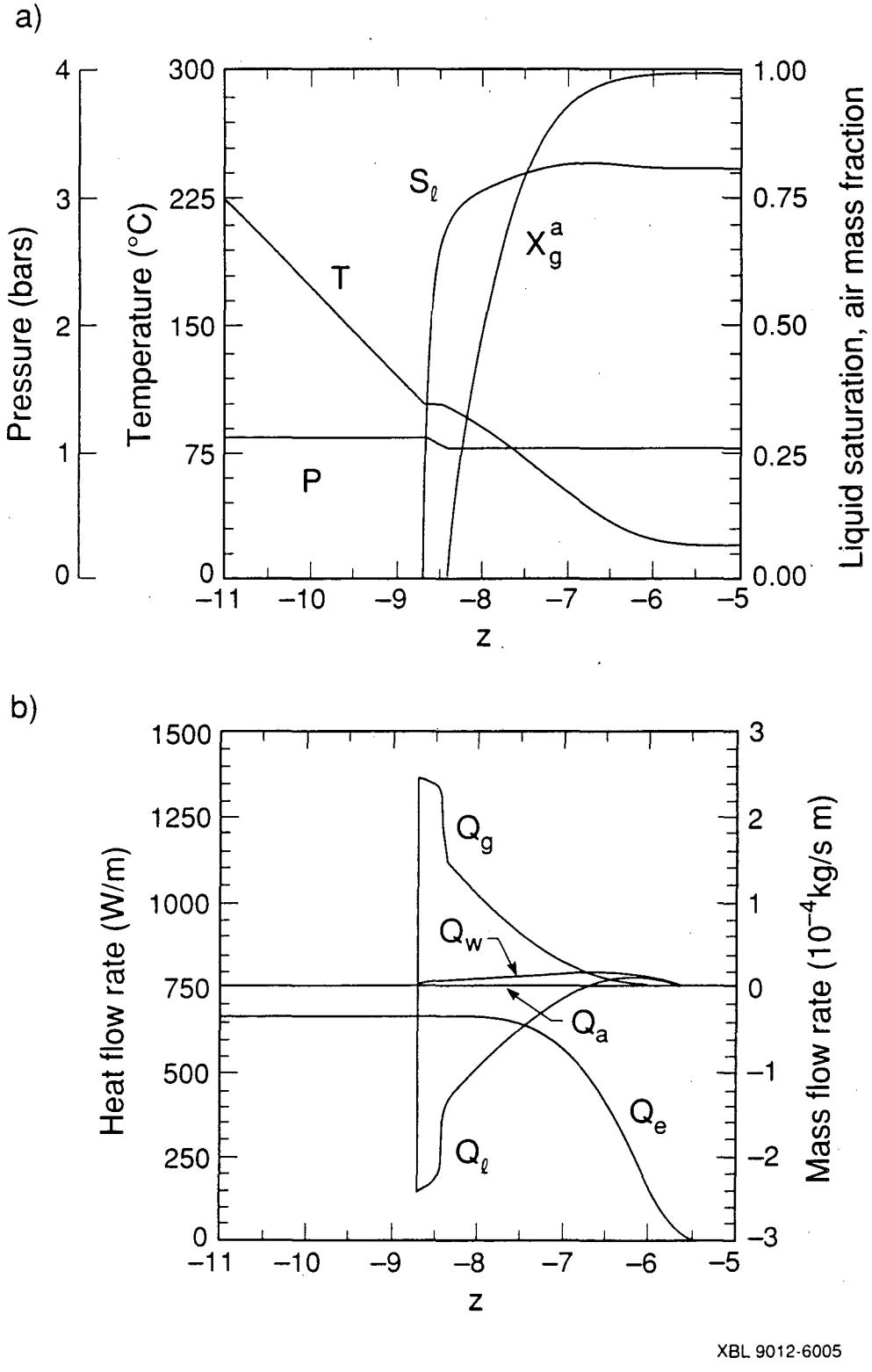

Figure 11. Results of the similarity solution for a problem with enhanced vapor diffusion ($\beta = 1$), with other properties given in Table 1.

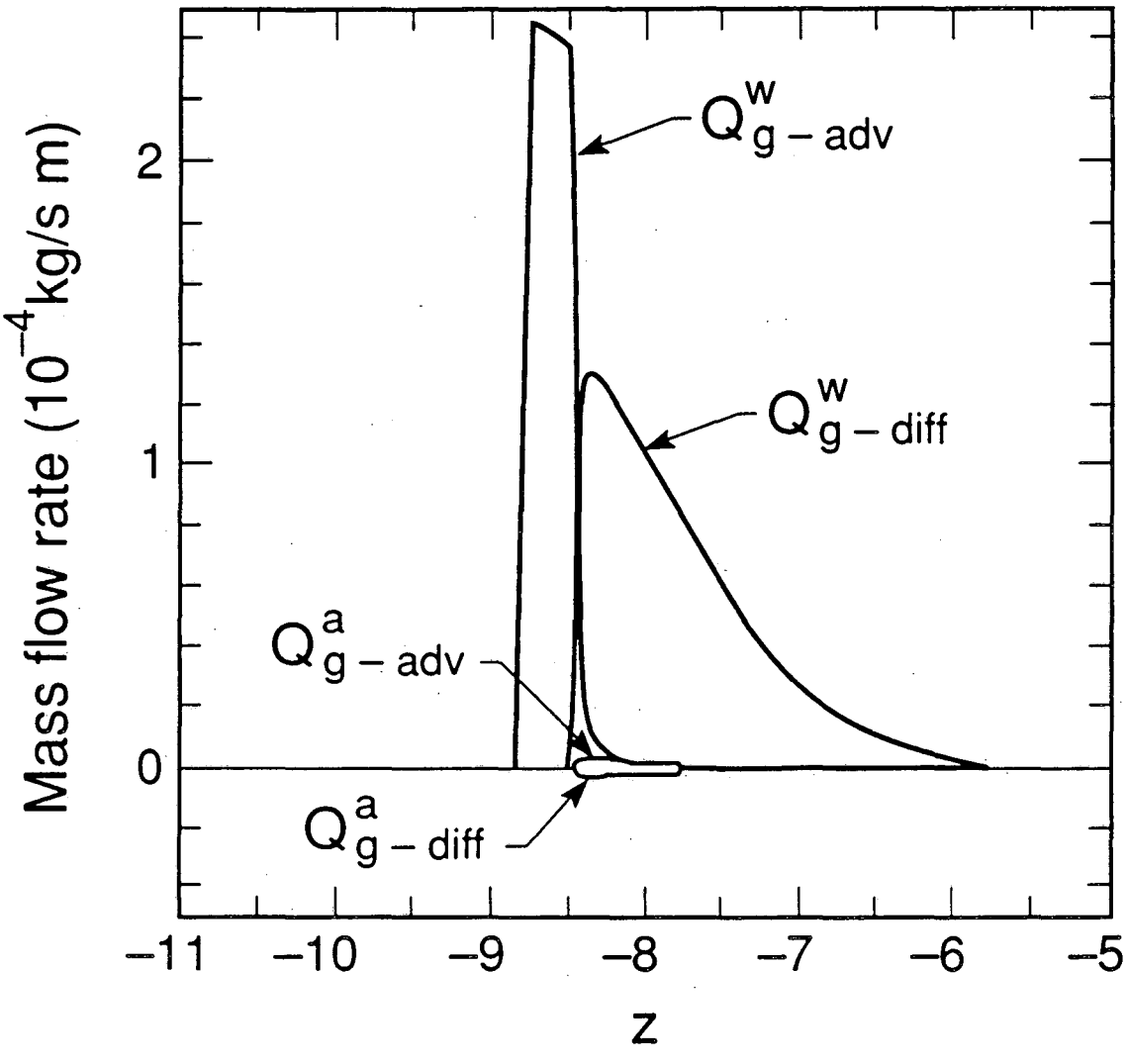

XBL 9012-6006

Figure 12 Diffusive (Q_{g-diff}) and advective (Q_{g-adv}) components of the gas-phase flows shown in Figure 11.

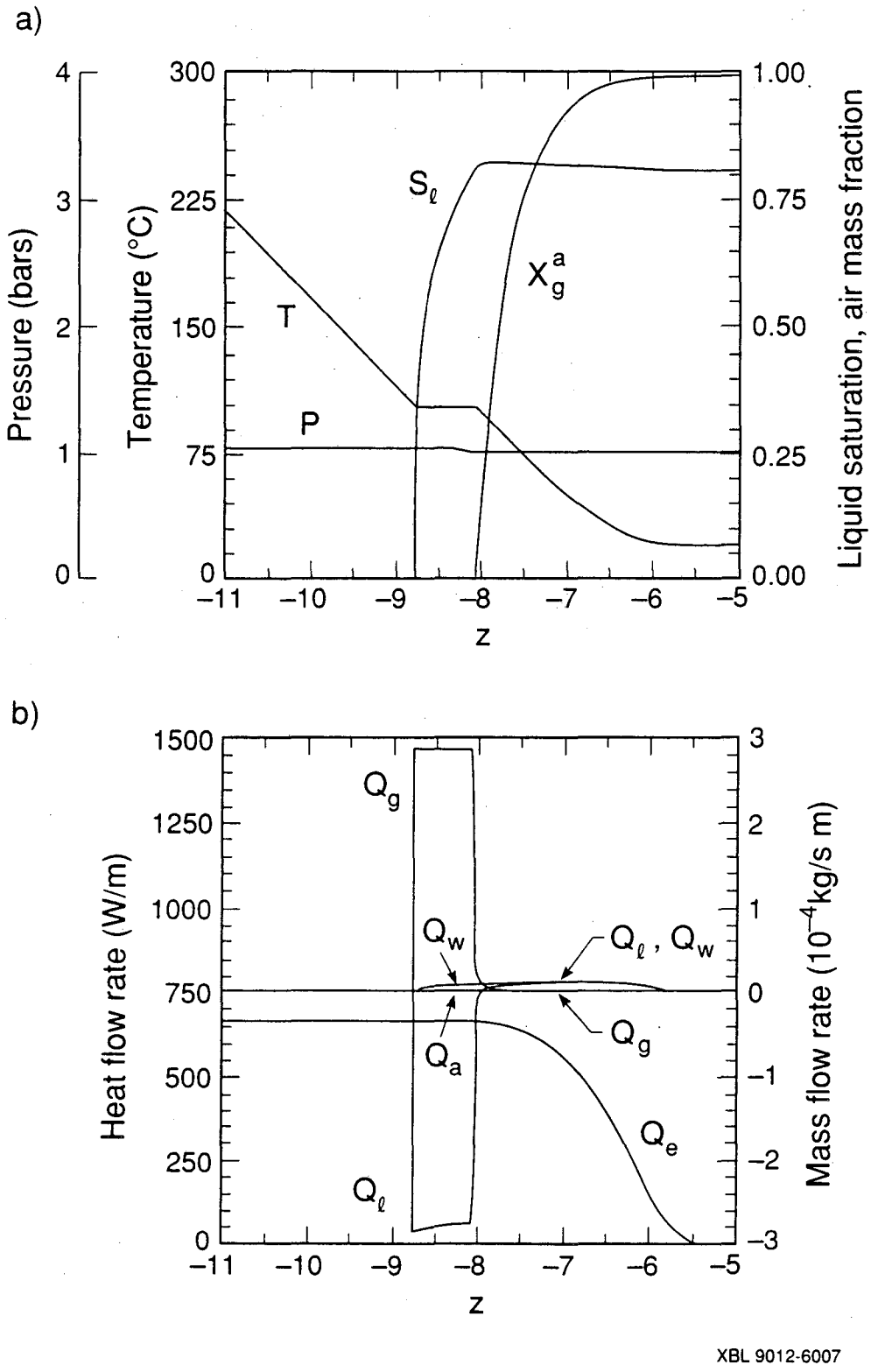

Figure 13. Results of the similarity solution for a problem with Knudsen diffusion given by $b = 7.6$ bars, with other properties given in Table 1.

LAWRENCE BERKELEY LABORATORY
UNIVERSITY OF CALIFORNIA
INFORMATION RESOURCES DEPARTMENT
BERKELEY, CALIFORNIA 94720